The X-ray constrained wavefunction of the $[Mn(CO)_4\{(C_6H_5)_2P–S–C(Br_2)–P(C_6H_5)_2\}]Br$ complex: A theoretical and experimental study of dihalogen bonds and other non-covalent interactions.

Authors

Juan F. Van der Maelen[a]*, Mario Ceroni[b] and Javier Ruiz[c]

[a]Dept. Química Física y Analítica, Universidad de Oviedo, Avda. Julián Clavería 8, Oviedo, Asturias, E-33006, Spain

[b]Facultad de Química e Ingeniería Química, Universidad Nacional Mayor de San Marcos, Lima, Peru

[c]Dept. Química Orgánica e Inorgánica, Universidad de Oviedo, Avda. Julián Clavería 8, Oviedo, Asturias, E-33006, Spain

Correspondence email: fvu@uniovi.es

Funding information Ministerio de Economía y Competitividad (contract No. MAT2016-78155-C2-1-R); Gobierno del Principado de Asturias (grant No. GRUP-IN-14-060); Ministerio de Ciencia e Innovación (contract No. PID2019-109975GB-100).

Synopsis The topology of the C–Br···Br dihalogen bond present in the title complex, as well as that of several non-covalent intramolecular C–H···Br–C interactions, have been studied from the point of view of the QTAIM and ELF methodologies applied to an X-ray constrained wavefunction.

Abstract The synthesis and X-ray structure determination of the $[Mn(CO)_4\{(C_6H_5)_2P–S–C(Br_2)–P(C_6H_5)_2\}]Br$ complex (**1**) are described in the current work. The C–Br···Br dihalogen bond present in **1** has been characterized by means of topological studies of the electron density. Both the Quantum Theory of Atoms in Molecules (QTAIM) and the Electron Localization Function (ELF) approaches have been applied to several theoretically calculated wavefunctions as well as to an X-ray constrained wavefunction (XCW). In addition, a number of theoretical techniques, like the Source Function (SF), the Reduced Density Gradient method (RDG) and the Interacting Quantum Atoms approach (IQA), among others, have been used to analyse the dihalogen bond as well as several intramolecular interactions of the type C–H···Br–C which have also been detected in **1**. The results show clearly that while bonding in the latter interactions are dominated by electrostatic components, the former has a high degree of covalency.

Keywords: halogen bonds; non-covalent interactions; Quantum Theory of Atoms in Molecules (QTAIM); Electron Localization Function (ELF); X-ray Constrained Wavefunction (XCW).

1. Introduction

The interest in halogen bonding has increased so incredibly in recent years that not only the International Union of Crystallography (IUCr) has sponsored several symposia on this subject since the first one in 2014 but even special issues of several journals have been devoted to this topic (i.e. Erdelyi & Metrangolo, 2017). According to the recommendations of the International Union of Pure and Applied Chemistry (IUPAC), "a halogen bond occurs when there is evidence of a net attractive interaction between an electrophilic region associated with a halogen atom in a molecular entity and a nucleophilic region in another, or the same, molecular entity" (Desiraju *et al.*, 2013). An R–X···B interaction between a halogen-bond donor (R–X) and an acceptor (B) is typically collinear with the R–X covalent bond (albeit exceptions do exist), has an internuclear distance less than the sum of van der Waals radii, and is usually slightly stronger than a hydrogen bond R–H···B (halogen bonding covers a large class of non-covalent interactions with strengths in the range 10–200 kJ mol^{-1}) (Metrangolo *et al.*, 2008; Cavallo *et al.*, 2016; Jelsch & Guillot, 2017). Although many studies have been published to date on this subject , starting from the very first example of an adduct formation between iodine and ammonia as early as in 1814 (Colin, 1814), there is still controversy on the exact nature of the halogen-bonding interaction. Not long ago the concept of a σ-hole bond, based on the molecular surface electrostatic potential, was proposed to characterize the halogen bond, thus emphasizing the electrostatic nature of the interaction (Clark *et al.*, 2007; Politzer *et al.*, 2010). A σ-hole is a region of positive electrostatic potential at the terminus of the R–X covalent bond, which is surrounded by a belt of negative potential. However, many authors have questioned the purely electrostatic nature of XB interactions (Gilday *et al.*, 2015; Wang *et al.*, 2016; Thirman *et al.*, 2018), showing that electrostatic, charge transfer, polarization, and dispersion contributions to the bonding in this kind of non-covalent interactions often depend upon the particular interacting atoms involved.

Dihalogen bonds, in which two halogen atoms are in contact, are substantially less studied than halogen bonds (Grabowsky, 2018). Similarly to the case of a dihydrogen bond, one of the halogen atoms may act as a Lewis acid centre while the other acts as a Lewis base centre, although both halogen atoms may reveal their dual acidic-basic character as well (Grabowsky, 2020). In order to check the possibility of observing a Br···Br contact into the same moiety we performed the synthesis and crystallization of the $[Mn(CO)_4\{(C_6H_5)_2P–S–C(Br_2)–P(C_6H_5)_2\}]Br$ complex (**1**) followed by the topological study of the non-covalent interactions here detected. The C–Br···Br dihalogen bond present in **1**, along with several intramolecular C–H···Br–C interactions found, deserved in our opinion a detailed analysis of this compound, since to the best of our knowledge this is the first study of simultaneous hydrogen and dihalogen bonding involving the *same* halogen atom in the *same* organometallic complex, thus giving us the opportunity to compare both kinds of interactions on the same basis. The synthesis of complex **1** is itself highly remarkable, as it implies an unprecedented insertion reaction of a sulphur atom into a strong P–C bond. In fact, there are only a handful of

reported examples of P–C bond insertions, which to date involve molecules such as nitriles, alkynes, or thiocyanogen (Schiffer & Scheer, 2001; Streubel *et al.*, 2000; Yamamoto & Sugawara, 2000; Ruiz *et al.*, 2007). The structure of **1**, showing a P–C–S–P expanded skeleton for the diphosphine ligand is also unique.

The topological study of the electron density was carried out by means of several combined experimental and theoretical approaches, involving different theoretically optimized geometries of **1** in gas phase as well as the X-ray experimental geometry (see below the 'Computational methodology' subsection of the 'Experimental section' for details). In particular, we have checked the feasibility of applying the so-called X-ray constrained wavefunction method (XCW) (Jayatilaka & Grimwood, 2001; Grimwood & Jayatilaka, 2001; Bytheway *et al.*, 2002;) to complex **1**, as an alternative to the more widely known multipolar refinement method (Hansen & Coppens, 1978; Coppens, 1997) for obtaining experimental electron densities, since XCW performs successfully even in the absence of a high resolution X-ray data set, as it has already been applied recently to medium resolution data sets (Grabowsky *et al.*, 2012; Dittrich *et al.*, 2012; Bučinský *et al.*, 2016; Woińska *et al.*, 2014, 2017, 2019), although undoubtedly the higher the better.

It has been previously shown that a single tool is not enough to fully characterize halogen bonds and, in particular, to properly distinguish them from hydrogen bonds of similar strength (Martínez-Amezaga *et al.*, 2010; Rowe & Ho, 2017; Bartashevich *et al.*, 2017, 2019). Consequently, and in order to shed some additional light on the nature of the bonding in these important class of interactions, we have used the Quantum Theory of Atoms in Molecules (QTAIM) (Bader, 1990; Popelier, 2000; Matta & Boyd, 2007) as well as the Electron Localization Function approach (ELF) (Becke & Edgecombe, 1990; Gatti & Macchi, 2012; Frenking & Shaik, 2014), which are two different and complimentary ways of partitioning the molecular electron density. As opposed to the Molecular Orbital (MO) theory, the QTAIM approach starts from the electron density (a real space function), which is an observable that may be obtained either from X-ray data or theoretical calculations (although some magnitudes cannot be obtained from the experimental electron density since they need the first- or second-order reduced density matrices), while the ELF approach is based on the conditional same-spin pair density. Both QTAIM and ELF methodologies, combined with other related to them, like the Source Function (SF) (Gatti & Lasi, 2007), the Reduced Density Gradient method (RDG), (Johnson *et al.*, 2010), and the Interacting Quantum Atoms approach (IQA) (Popelier & Kosov, 2001; Blanco *et al.*, 2005) have been applied so far to a plethora of organometallic compounds, with and without transition metals, giving unambiguous, stable, and robust results, which are almost independent of the model chemistry used (i.e, method of calculation, density functional and basis set) (see, for instance, Gatti, 2005, and references therein).

2. Experimental

2.1. Synthesis and structure determination of complex 1

The detailed experimental procedure for the synthesis, crystallization, and structural characterization of **1** (FTIR, NMR, and single-crystal Xray diffraction) is given in the Supporting Information. The synthesis of the starting compound ([$(CO)_4Mn\{(Ph_2P)_2C\text{-}S_2\text{-}C(PPh_2)_2\}Mn(CO)_4$]) has been described previously (Ruiz *et al.*, 2001). Selected crystallographic data and structure refinement parameters are given in Table 1, while Fig. 1shows the experimental molecular structure together with the atomic numbering scheme and selected bond lengths and angles.

Table 1

Crystallographic data of complex **1**.

Crystal data	
Chemical formula	$C_{29}H_{20}Br_3MnO_4P_2S$
CCDC No.	2006886
M_r	821.12
Crystal system, space group	Monoclinic, *C*2
Temperature (K)	293
a, *b*, *c* (Å)	15.366 (2), 16.035 (2), 14.327 (1)
β (°)	91.21 (1)
V (Å^3)	3529.3 (7)
Z	4
Radiation type	Mo *K*α
μ (mm^{-1})	3.95
Crystal size (mm)	0.26 × 0.23 × 0.10
Data collection	
Diffractometer	Bruker APEX-II
Absorption correction	Multi-scan
T_{min}, T_{max}	0.528, 0.996
No. of measured, independent and observed [$I > 2\sigma(I)$] reflections	3749, 3603, 2399
R_{int}	0.057
θ values (°)	θ_{max} = 26.0, θ_{min} = 1.4
$(\sin\theta/\lambda)_{max}$ (Å^{-1})	0.616
Range of *h*, *k*, *l*	*h* = −18→18, *k* = 0→19, *l* = −17→0
Refinement	
$R[F^2 > 2\sigma(F^2)]$, $wR(F^2)$, *S*	0.046, 0.127, 0.99
No. of reflections	3603
No. of parameters	361
No. of restraints	1
H-atom treatment	H-atom parameters constrained
$(\Delta/\sigma)_{max}$	0.001

$\Delta\rho_{max}$, $\Delta\rho_{min}$ (e Å^{-3})	0.68, −0.49
Absolute structure	No quotients, so Flack parameter determined by classical intensity fit
Absolute structure parameter	0.040 (14)

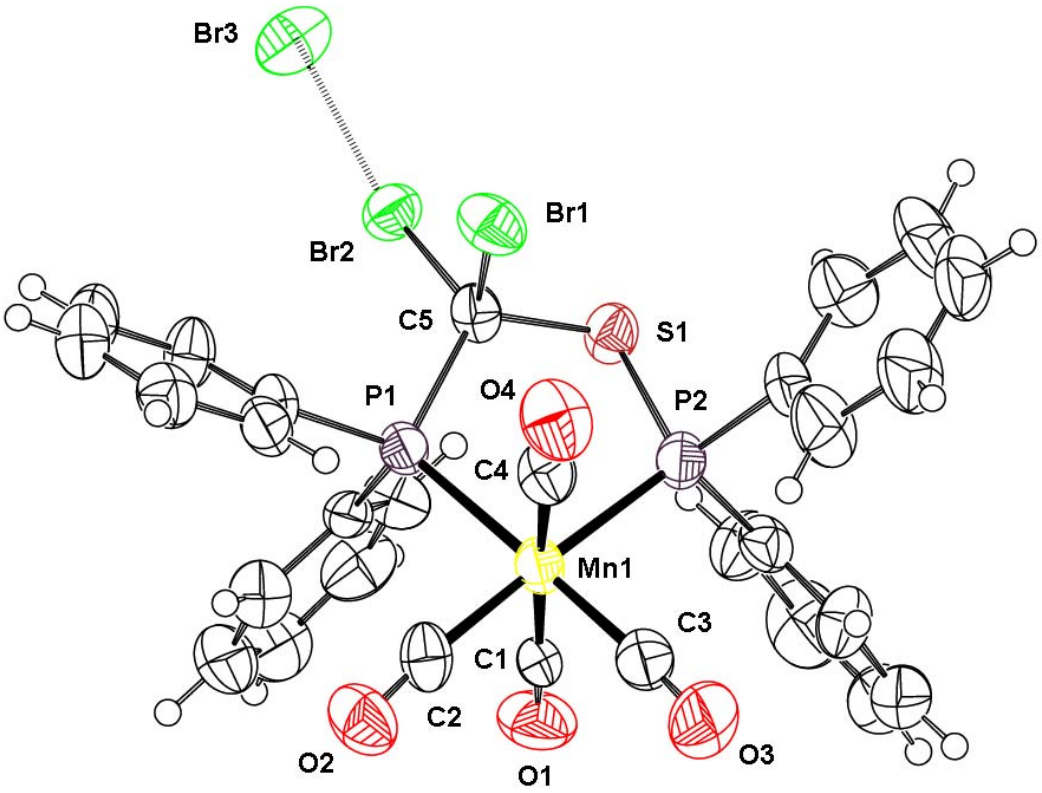

Figure 1

Molecular structure of complex **1** showing the atomic numbering scheme for selected atoms (displacement ellipsoids at 50% probability). Selected bond distances (Å): Mn1−P1, 2.340(3); Mn1−P2, 2.321(3); P1−C5, 1.868(9); P2−S1, 2.118(3); S1−C5, 1.786(9); C5−Br1, 1.978(9); C5−Br2, 1.989(9); Br2−Br3, 3.083(2). Selected bond angles (°): Mn1−P1−C5, 108.0(3); Mn1−P2−S1, 111.6(1); P1−C5−S1, 114.0(5); P2−S1−C5, 99.9(3); P1−C5−Br1, 105.1(4); P1−C5−Br2, 116.7(5); S1−C5−Br1, 111.3(5); S1−C5−Br2, 103.8(4); Br1−C5−Br2, 105.7(4); C5−Br2−Br3, 172.2(3).

2.2. Computational methodology

Four different models have been used in the current study (see footnote in Table 2), two of them with the X-ray experimental geometry and another two with theoretically optimized geometries in gas phase (tables of coordinates are given in the Supporting Information: Tables S1, S2, and S3). Theoretically optimized geometries were obtained using two different methods: the non-relativistic B3P86-D3(BJ)/6-31G(d,p) and the relativistic ZORA-BLYP-D3(BJ)/TZP. A zero-order relativistic Hamiltonian (ZORA), coupled with the hybrid M06-2X density functional (Zhao & Truhlar, 2008), with all-electron QZ4P basis sets for all atoms (including Mn and Br atoms), and utilizing dispersion corrections with Becke-Johnson damping (Grimme *et al.*, 2011), as implemented in the *ADF2012* program package (Baerends *et al.*, 2012), were used for single-point electronic structure calculations at the relativistically optimized geometry (model 1 hereafter). Similarly, for the non-relativistically optimized geometry, the method M06-D3/QZVP was used (model 2 hereafter), which includes, together with a three-parameter empirical dispersion and the hybrid M06 density functional, the all-electron QZVP basis set for all atoms, as implemented in the *GAUSSIAN09* program package (Frisch *et al.*, 2009).

The latter method has also been used to perform single-point electronic structure calculations at the X-ray experimental geometry (model 3 hereafter). The last model (model 4 hereafter) also uses the experimental geometry but in a very different way: an 'experimental' wave function has been calculated by means of the X-ray constrained wavefunction method (XCW) as implemented in the *TONTO* software (Jayatilaka & Grimwood, 2003). The XCW method optimizes the Lagrangian *L*, given by

$$L = E[\Psi] - \lambda_{XCW}[\chi^2 - \chi^2_0]$$

where the first term is the quantum mechanical energy (as obtained from the wavefunction itself), which is the function to be minimized subject to the condition given by the second term, where λ_{XCW} is the Lagrange multiplier; that is, the experimental least-squares error in terms of the χ^2 agreement statistics (the condition to be fulfilled by the optimization procedure is $\chi^2 = \chi^2_0$), with χ^2 also a function of Ψ. The Lagrange multiplier must be determined iteratively *and* interactively, but it does not have any real physical meaning, more than the relative weight given to the experimental data in the optimization procedure (Macchi, 2013). Although it has been shown that a Hirshfeld atom refinement procedure (HAR) previous to XCW greatly increases both the convergency speed and the accuracy of the final wavefunction (Jayatilaka & Dittrich, 2008), the so-called combined HAR-XCW

method (also called XRW) proved unsuccessful in the current study due probably to the modest resolution achieved in the X-ray data collection (see Table 1), which prevented the HAR refinement from convergency. Using the method B3LYP/6-31G(d,p), with fixed atomic charges and dipoles on surrounding molecules within a radius of 8 Å, the XCW procedure finally converged to a value of $\lambda_{XCW} = 0.540$, with $\chi^2 = 3.241$.

The obtained ground-state electronic wavefunctions, which were found to be stable, were then used for the QTAIM, ELF, and NBO calculations, which included both local and integral topological properties and were carried out with the *AIMAll* (Keith, 2015), *AIM2000* (Biegler-König & Schönbohm, 2002), *DGrid* (Kohout, 2011), *Multiwfn* (Lu & Chen, 2012), *Chimera* (Pettersen *et al.*, 2004), and *NBO* (Glendening *et al.*, 2018) program packages. The accuracy of the local topological properties was finally set at 1.0×10^{-10} au (from the gradient of the electron density at bond critical points), while that of the integral topological properties was established at a minimum of 1.0×10^{-4} au (from the Laplacian of the integrated electron density).

3. Results and discussion

The images in Fig. 2 show the molecular graph of complex **1** obtained using model 4 (similar images are obtained using the other three models), with the complete set of bond critical points (*bcps*) and ring critical points (*rcps*), as well as bond paths (*bps*) connecting bonded atoms through their corresponding *bcps*. Apart from the covalent C5−Br2 bond, three other interactions involving the Br2 atom are revealed in Fig. 2b, i.e. Br2···Br3, Br2···H7, and Br2···H13. From an orthodox QTAIM point of view, the presence of a *bp* and a *bcp* between two atoms is a necessary and sufficient condition for the existence of a bonding interaction between both atoms (Bader, 1990), although it is well known that alternative interpretations are also possible, in particular when weak interactions are involved (Shahbazian, 2018). In this sense, it should be emphasized that the presence of *solely* Br2···H *bcps* and *bps* are not definitive signs of non-covalent interactions between those atoms in **1**, although they may be used to confirm the existence of such interactions if they are additionally revealed by other procedures, like non-covalent index (NCI) methods (Van der Maelen, 2020). One additional feature that may be appreciated in Fig. 2b that clearly distinguishes between Br···Br and Br···H interactions in **1** is that whereas the Br2···Br3 *bp* is a perfectly straight line with the *bcp* located not far from the midpoint of the *bp*, both Br2···H7 and Br2···H13 *bps* are clearly curved, with *bcps* much closer to their corresponding hydrogen atoms than to the Br2 atom (the Supporting Information gives, in Table S4, the exact Br2−*bcp* and *bcp*−X distances, with X = Br3, H7, and H13). As a consequence, the Br2···Br3 bond path length (*bpl*) is almost identical to its interatomic distance while Br2···H7 and Br2···H13 *bpls* are higher than their interatomic distances (see below for a more quantitative discussion of this point).

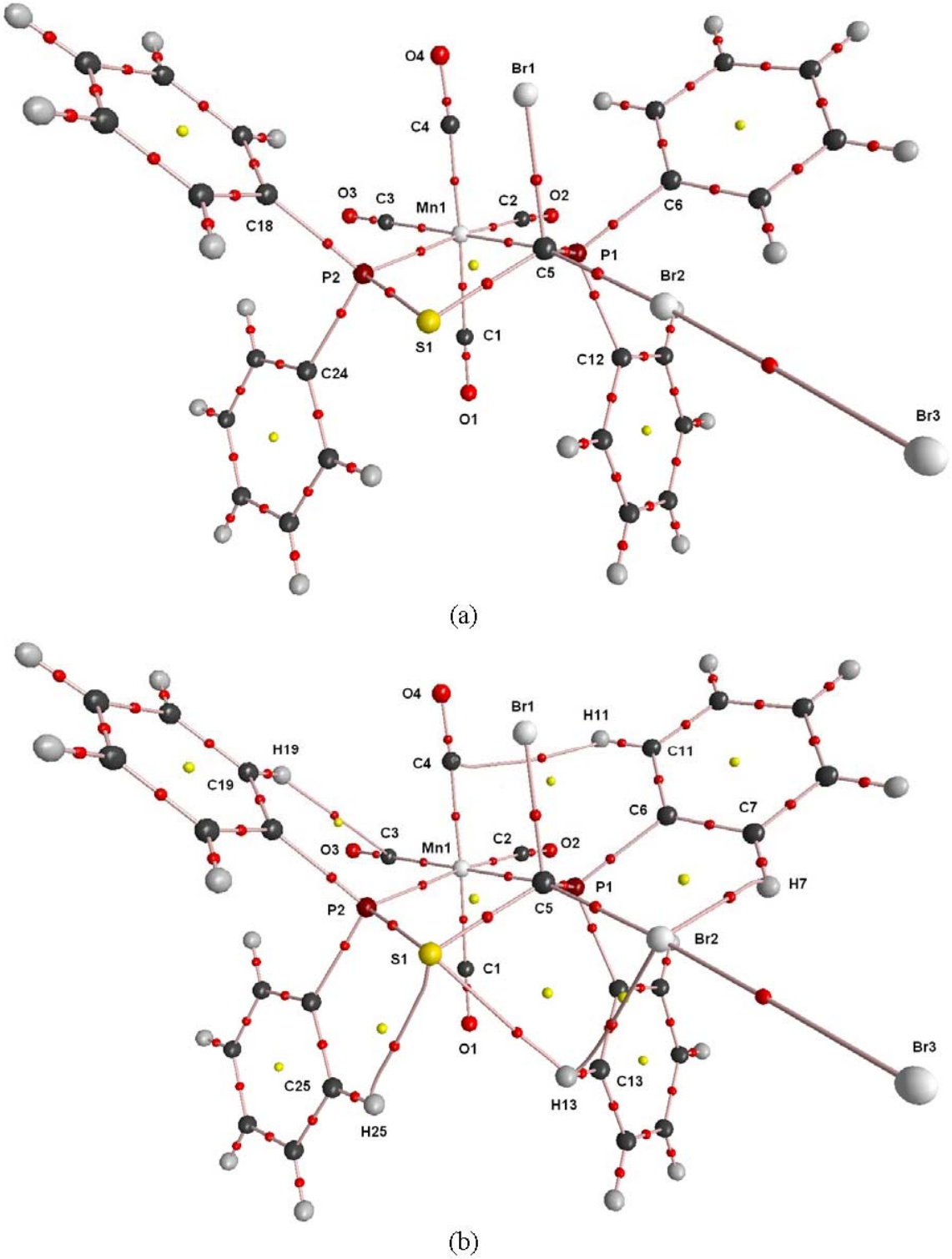
O4
Br1
C4
O3
C3
Mn1
C2
O2
C6
C18
P1
P2
C5
Br2
S1
C1
C12
C24
O1
Br3
(a)
O4
Br1
H11
C11
H19
C4
C19
C6
C7
C3
O3
Mn1
C2
O2
P1
H7
P2
C5
Br2
S1
C1
O1
Br3
C25
C13
H13
H25
(b)

Figure 2

Molecular graph of complex **1** showing bond critical points (small red spheres) and ring critical points (small yellow spheres), as well as bond paths (thin lines), including: (a) only covalent bonds and the Br2···Br3 interaction, and (b) also all weak non-covalent interactions detected.

In Fig. 3, a gradient trajectory map of the total electron density in the Br1−Br2−Br3 plane of complex **1**, calculated using model 4, is shown (similar images are obtained using the other three models). Atomic basins of C5, Br1, Br2, and Br3 atoms are displayed (with the former atom located slightly out of plane), together with *bps* and *bcps* located in the same plane or slightly out of plane. Integration of the electron density inside each atomic basin rendered the electric charge, *Q*, of each atom. Table 2 collects the QTAIM electric charge of selected atoms in **1** using the four models considered in the current study. By means of a comparison, the QTAIM electric charge obtained for the Mn atom in other carbonyl complexes having this metal, and using equivalent calculation methods, vary from 0.9 e to 1.1 e (Van der Maelen & Cabeza, 2016; Brugos *et al.*, 2017), with values in Table 2 within this range for Mn1. In addition, the four models give quite similar results for S1, C5, Br1, and Br2 electric charges, with $Q < 0.1$ e for the latter atom. On the other hand, for the Br3 atom there is a slight difference between models 1 and 2 (theoretically optimized geometries), on one side, and models 3 and 4 (experimental geometry), on the other side, giving values around, respectively, −0.5 e and −0.7 e (see Table 2). Rather interestingly, the former two models give positive values for the charge of both H7 and H13 atoms, whereas the latter two models give negative values for the same charges, slightly higher (in absolute value) in model 4 than in model 3. The Coulomb electrostatic potential (ESP), represented in Fig. 4, is even more informative than monopolar charges alone, since it includes multipolar expansion terms, and it clearly shows here a characteristic σ-hole for the C–Br···Br dihalogen interaction present in **1**. All in all, these results are consistent with a significant electrostatic contribution to the Br2···Br3 interaction in the current complex.

Table 2

QTAIM atomic charges, *Q* (e), for selected atoms of complex **1**, calculated using the four models.

Model[†]	Mn1	S1	C5	Br1	Br2	Br3	H7	H13
1	+0.8759	−0.1602	−0.6901	−0.1211	+0.0411	−0.4900	+0.0532	+0.0424
2	+0.8634	−0.1738	−0.7042	−0.1070	+0.0567	−0.4961	+0.0530	+0.0425
3	+0.8632	−0.1801	−0.6108	−0.0874	+0.0800	−0.7403	−0.0910	−0.1066
4	+1.0230	−0.1073	−0.6845	−0.1138	+0.0277	−0.7832	−0.2312	−0.2317

[†]Models: ZORA-BLYP-D3(BJ)/TZP//ZORA-M06-2X/QZ4P (*model 1*), B3P86-D3(BJ)/6-31G(d,p)//M06-D3/QZVP (*model 2*), exp-geom//M06-D3/QZVP (*model 3*), exp-geom//XCW-B3LYP/6-31G(d,p) (*model 4*).

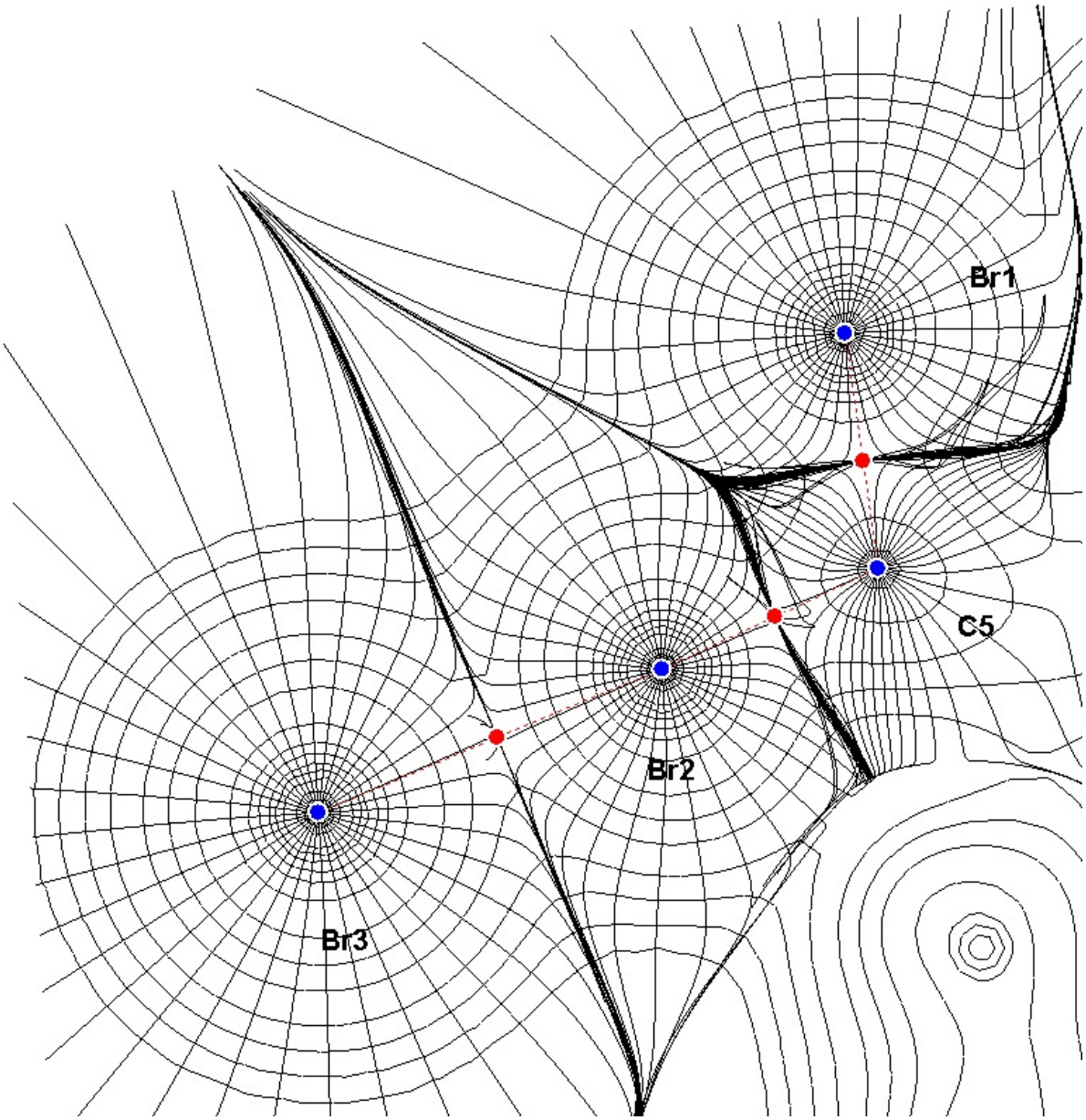

Figure 3

Gradient trajectories mapped on a total electron density plot (contour levels at 0.1 e Å^{-3}) in the Br1−Br2−Br3 plane of complex **1**, showing atomic basins, stationary points (blue circles), *bps* (dashed red lines), and *bcps* (red circles).

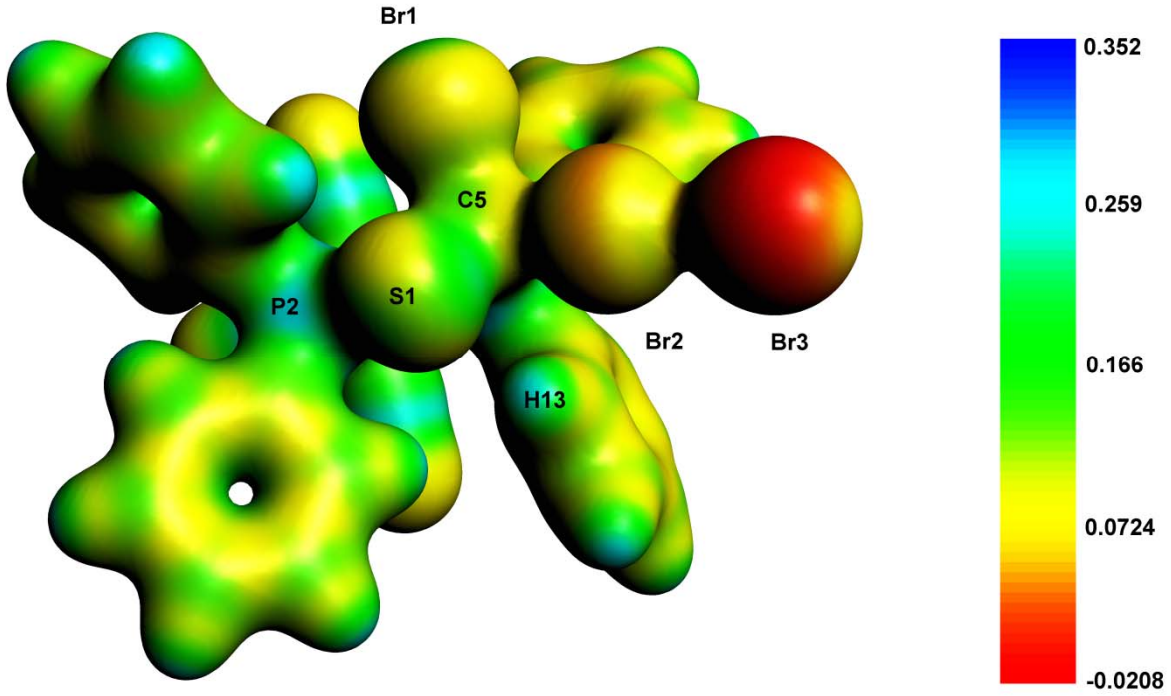

Figure 4

Electrostatic potential (au) mapped on a 0.03 e $Å^{-3}$ electron density isosurface of **1** calculated using model 1.

Local topological properties of the electron density (i.e., those calculated at a *bcp*) have been frequently used to successfully analyse the bonding in all kinds of compounds, particularly those containing metal atoms. The electron density (ρ_b), the ellipticity (ε_b), the Laplacian of the electron density ($\nabla^2\rho_b$), the kinetic energy density ratio (G_b/ρ_b), and the total energy density ratio (H_b/ρ_b, with $H(r) = G(r) + V(r)$ and $1/4\nabla^2\rho(r) = 2G(r) + V(r)$, where V(r) is the potential energy density) are the most common of those properties. Generally speaking, local topological properties are related to the strength and nature of the interactions for which a *bcp* is present and may be used to classify bonds between the traditional chemical categories; i.e. closed-shell vs. open-shell, as well as to distinguish between pure covalent, polar-covalent, dative, and ionic bonds, among others. A typical non-covalent interaction, like a weak or medium-strength hydrogen bond or a halogen bond of the same strength, has a small value of ρ_b, a positive small value of $\nabla^2\rho_b$, and a close-to-zero value of H_b/ρ_b (Martínez-Amezaga *et al.*, 2010; Grabowsky, 2011). In addition, the balance between G_b and V_b reveals in part the nature of these interactions: when $|V_b|/G_b < 1$ the interaction is purely non-covalent, whereas if $2 > |V_b|/G_b > 1$ some covalent component is involved (Espinosa *et al.*, 2002).

In Table 3, values of the above mentioned local topological properties for selected interactions in complex **1**, calculated using the four theoretical models, are included. By taking the C5−Br1 bond

(first entry in Table 3) as a typical covalent bond between different non-metal atoms, and the S1···H13 interaction (last entry in Table 3) as a typical hydrogen bond, several interesting comparisons may be made among the other interactions included in Table 3. Both Br2···H7 and Br2···H13 interactions show values close to the ones for the S1···H13 interaction, as expected. The small (< 0.1) values of ρ_b, added to the small (< 1) positive values of $\nabla^2\rho_b$, the small (<1) positive values of H_b/ρ_b, and the less-than-one values of G_b/ρ_b, shown by Br2···H7 and Br2···H13 interactions, are typical of weak hydrogen bonds of a high electrostatic nature. Nevertheless, these two bonds are not completely identical to the S1···H13 interaction, as differences in ellipticity between hydrogen bonds involving the Br2 atom and the S1 atom are apparent in Table 3. In addition, there is a higher curvature in Br2···H7 and Br2···H13 *bps* than in the S1···H13 *bp*. By using model 1, for instance, the difference between the *bpl* and the interatomic distance is only 0.04 Å for the S1···H13 interaction, whereas it is 0.16 Å and 0.10 Å, respectively, for Br2···H7 and Br2···H13 interactions, which indeed means that the latter *bps* are much more curved than the former. On the contrary, for the Br2···Br3 interaction the interatomic distance and the *bpl* are almost identical to each other (see Table S4 in the Supporting Information), thus the *bp* shows no curvature at all, which added to an almost zero ellipticity leads to a basically cylindrical straight bond path. The other local topological parameters included in Table 3 for the Br2···Br3 interaction also show significant differences as compared to the ones exhibited by Br2···H7 and Br2···H13 interactions. In particular, the fact that $H_b/\rho_b < 0$ (and hence $|V_b|/G_b > 1$) for the first two models (and basically zero for the other two) is a clear sign that the dihalogen bond present in **1** is not pure closed-shell, but instead a non-negligible covalent contribution must be taken into account to explain this bonding. Rather surprisingly, data in Table 3 for the C5−Br2 bond in gas phase (models 1 and 2) shows more similarities with the Br2···Br3 interaction than with the C5−Br1 pure covalent bond, which is undoubtedly due to the fact that the theoretical C5−Br2 bond distance is clearly longer than the theoretical C5−Br1 bond distance, while the experimental ones are almost identical (compare *bpls* in the second column of Table 3 with experimental distances in Fig. 1). For instance, the C5–Br2 *bcp* in the gas phase (models 1 and 2) is located in the positive region of the Laplacian, whereas it is located in the negative region in the solid state (models 3 and 4). Therefore, in gas phase the C5–Br2 interaction seems to be closer to a halogen bond than to a typical covalent bond between different non-metal atoms (see below for further discussion on this point). The intermediate ($0.1 < \rho_b < 0.5$) values of ρ_b, added to the small (≈ 1) positive values of $\nabla^2\rho_b$, the close-to-zero or very small negative values of H_b/ρ_b, and the less-than-one values of G_b/ρ_b, shown in Table 3 for the Br2···Br3 interaction, are typical of either polar-covalent or dative bonds (Grabowsky, 2011). Although these data are within the values shown by typical strong halogen bonds (Martínez-Amezaga *et al.*, 2010), quite similar behaviour has also been observed, for instance, in M−X bonds (M = Transition metal, X = Halogen), like the Mo−Cl and Mo−Br interactions in $[Mo_2Cl_8]^{4-}$, $[Mo_2(\mu{-}Cl)_3Cl_6]^{3-}$, $[Mo_2(\mu{-}CH_3CO_2)_4Br_2]^{2-}$, and $[Mo_2(\mu{-}CF_3CO_2)_4Br_2]^{2-}$, among others (Van der Maelen & Cabeza,

2012), and even in several M−H bonds in many other instances (see, for example, Cabeza, Van der Maelen & García-Granda, 2009; Van der Maelen, García-Granda & Cabeza, 2011; Cabeza *et al.*, 2013; Van der Maelen & García-Granda, 2015; Van der Maelen & Cabeza, 2016; Brugos et al., 2016, 2017; Van der Maelen *et al.*, 2020).

However, it is well known that integral indexes are even more useful than local indexes for characterizing weak and very weak interactions, particularly in compounds containing metal atoms (Gatti, 2005). Integral topological properties are calculated along a bond path, over an interatomic surface or over a whole atomic basin. Among them, the delocalization index (DI), δ(A–B), which can be considered a covalent bond order measure since it is directly related to the number of electron pairs shared between atoms A and B, is by far the integral index that has been most frequently used. For pure covalent bonds, like a C−C interaction, the value of DI is approximately equal to the formal bond order. In Table 3 (last column), where δ(A–B) values of the selected interactions mentioned above are included, data for both C5−Br1 and C5−Br2 bonds are representative of single covalent bonds without delocalization, as expected. On the other hand, the low values of DI ($\delta \leq 0.05$) for Br2···H7, Br2···H13, and S1···H13 bonds are typical of interactions with a low degree of covalency (i.e. dominated by electrostatics). On the contrary, values for δ(Br2···Br3) in **1** clearly show a much higher degree of covalency, which can be estimated to be between 45% (models 3 and 4) and 80% (models 1 and 2), depending on the molecular geometry used (experimental or theoretical, respectively), and assuming a DI value of one for a formal bond order of one in a pure covalent 2c-2e bond without delocalization (see below for a more quantitative discussion on this point).

An additional integral topological property that may be used for characterizing bonding interactions is the integrated electron density over the whole interatomic surface, $\int_{A\cap B}\rho$, which is related to the bond strength (Gatti, 2005). Table 4 collects values of this property for selected interactions in **1**, showing that it is between four and five times higher for the Br2···Br3 interaction than for Br2···H7, Br2···H13, and S1···H13 interactions, and then clearly stronger for the former. In fact, the Br2···Br3 bond is not particularly weak, since the value of $\int_{Br2\cap Br3}\rho$ is of the same magnitude of that found in typical donor-acceptor bonds with a moderate charge transfer, like, for instance, the Zn−C bond in $Zn_2(\eta^5\text{-}C_5Me_2)_2$, for which $\int_{Zn\cap C}\rho$ is, on average, 0.254 e $Å^{-1}$ (Van der Maelen *et al.*, 2007) or the Mo−Br bond in $[Mo_2(\mu{-}CH_3CO_2)_4Br_2]^{2-}$ and $[Mo_2(\mu{-}CF_3CO_2)_4Br_2]^{2}$, where $\int_{Mo\cap Br}\rho$ is, respectively, 0.610 e $Å^{-1}$ and 0.869 e $Å^{-1}$ (Van der Maelen & Cabeza, 2012). In addition, $\int_{Br2\cap Br3}\rho$ values for models 1 and 2 are more than twice than those for models 3 and 4, showing that this interaction is definitely stronger for the complex in gas phase than in the crystal.

Table 3

Topological parameters of selected interactions in complex **1**, calculated using the four models†.

Interaction	d (Å)[a]	ρ_b (e Å^{-3})[b]	$\nabla^2\rho_b$ (e Å^{-5})[c]	H_b/ρ_b (h e^{-1})[d]	G_b/ρ_b (h e^{-1})[e]	ε_b[f]	δ(A–B)[g]
C5−Br1	2.005	0.912	−2.012	−0.518	0.364	0.059	1.058
	1.969	0.972	−2.458	−0.552	0.375	0.062	1.078
	1.979	0.966	−2.386	−0.542	0.370	0.036	1.058
	1.977	0.921	−1.942	−0.512	0.364	0.014	1.038
C5−Br2	2.239	0.580	1.000	−0.333	0.454	0.036	0.698
	2.191	0.632	0.896	−0.369	0.468	0.037	0.725
	1.989	0.942	−1.236	−0.539	0.447	0.026	0.984
	1.989	0.920	−1.316	−0.515	0.418	0.016	0.985
Br2···Br3	2.626	0.407	1.381	−0.218	0.455	0.002	0.813
	2.558	0.462	1.366	−0.265	0.472	0.002	0.845
	3.084	0.163	1.147	0.005	0.488	0.004	0.448
	3.084	0.166	1.215	0.004	0.537	0.135	0.460
Br2···H7	3.026	0.061	0.629	0.101	0.613	0.240	0.040
	2.992	0.073	0.759	0.098	0.635	0.367	0.042
	3.045	0.060	0.655	0.109	0.653	0.223	0.039
	2.997	0.063	0.735	0.161	0.650	0.277	0.051
Br2···H13	3.072	0.068	0.740	0.107	0.653	0.513	0.036
	2.953	0.076	0.812	0.094	0.653	0.408	0.043
	3.261	0.054	0.648	0.137	0.702	0.478	0.026
	3.221	0.055	0.696	0.191	0.694	0.913	0.031
S1···H13	2.674	0.091	0.894	0.063	0.624	0.080	0.054
	2.783	0.076	0.781	0.082	0.632	0.046	0.045
	2.808	0.070	0.759	0.096	0.658	0.082	0.044
	2.801	0.077	0.846	0.115	0.654	0.071	0.054

†Models: ZORA-BLYP-D3(BJ)/TZP//ZORA-M06-2X/QZ4P (*model 1*, first row of each entry), B3P86-D3(BJ)/6-31G(d,p)//M06-D3/QZVP (*model 2*, second row of each entry), exp-geom//M06-D3/QZVP (*model 3*, third row of each entry), exp-geom//XCW-B3LYP/6-31G(d,p) (*model 4*, fourth row of each entry). [a]Bond path length. [b]Electron density at the *bcp*. [c]Laplacian of the electron density at the *bcp*. [d]Total energy density ratio at the *bcp*. [e]Kinetic energy density ratio at the *bcp*. [f]Ellipticity at the *bcp*. [g]Delocalization index.

Table 4

Electron density integrated over the interatomic surface, $\int_{A\cap B}\rho$ (e Å^{-1}), for selected interactions of complex **1**, calculated using the four models.

Model[†]	C5−Br1	C5−Br2	Br2···Br3	Br2···H7	Br2···H13	S1···H13
1	2.0798	1.3844	1.0356	0.1618	0.1782	0.1924
2	2.2074	1.4696	1.1456	0.2024	0.1982	0.1672
3	2.2654	2.0503	0.5361	0.1434	0.1062	0.1742
4	2.2675	2.0479	0.5374	0.1646	0.1206	0.2003

[†]Models: ZORA-BLYP-D3(BJ)/TZP//ZORA-M06-2X/QZ4P (*model 1*), B3P86-D3(BJ)/6-31G(d,p)//M06-D3/QZVP (*model 2*), exp-geom//M06-D3/QZVP (*model 3*), exp-geom//XCW-B3LYP/6-31G(d,p) (*model 4*).

Another integral property that can be calculated from QTAIM atomic basins is the Source Function (SF), which represents the contribution, in percentage, of each atomic basin of the molecule to the electron density at any particular point of the space (for instance, at a *bcp*) (Gatti, 2005). In Table 5, the SF% of selected atoms at several *bcps* is included for complex **1**, calculated using two different models (models 1 and 4), with equivalent results obtained by using the other two models. Not surprisingly, between 75% and 85% of the contribution at both C5−Br1 and C5−Br2 *bcps* comes from the two bonded atoms, with only very small contributions from other atoms, like S1 (~5%) and the other bromine atom (Br2 and Br1, respectively, ~ 5%), which are the other major contributions (other minor contributions are not included in Table 5). This is a well-known result for covalent bonds, which has been found previously in many instances (Gatti & Lasi, 2007; Ruiz *et al.*, 2019). Rather interestingly, for the Br2···Br3 interaction as well, more than 85% of the contribution comes from both bonded atoms, like in typical covalent bonds. On the contrary, the negative SF contribution of both S1 and H13 atoms to the electron density at the S1···H13 *bcp*, where both atoms act as sinks instead of as sources, is a clear sign of an interaction dominated by electrostatics. In addition, the fact that in both Br2···H7 and Br2···H13 interactions one of the bonded atoms acts as a source (the bromine atom, positive contribution) and the other as a sink (the hydrogen atom, negative contribution) shows again that these two interactions are not completely equivalent to the S1···H13 interaction.

An alternative but related way to study the nature of bonding interactions is the calculation of bond orders. For pure covalent bonds, the delocalization index (Table 3) is usually very close to Mayer's fuzzy bond order (FBO) and identical to the formal bond order, but they quantitatively differ for polar bonds. FBO is essentially the DI calculated in fuzzy atomic space (Mayer & Salvador, 2004). Commonly the magnitude of FBO is close to the usual Mayer bond order (Mayer, 2016), especially for low-polar bonds, but much more stable with respect to the change in basis set. Analogously, the

widely used Wiberg bond order (WBO) tends to overestimate bond order for polar bonds with reference to conventional Mayer's bond order (Wiberg, 1968). In Table 6 these three types of bond order are shown for the non-covalent interactions observed in complex **1**, calculated using models 1 (theoretical geometry) and 4 (experimental geometry), with equivalent results for the other two models. As may be seen in Table 6, values for the Br2···Br3 interaction clearly show a high degree of covalency, in spite of the fact that substantial differences between MBO values and both FBO and WBO values have been found, which can be associated to its substantial polarity, as explained above. On the contrary, the low values of the three bond indexes in Table 6 for Br2···H7, Br2···H13, and S1···H13 bonds, which closely resemble those of their DI's in Table 3, are typical of interactions with a low degree of covalency.

Table 5

SF contributions (%) of several atoms to the electron density at the *bcp* of selected interactions in complex **1**, calculated using two different models[†].

Interaction	C5	Br1	Br2	Br3	S1	H7	H13
C5−Br1	33.63	50.45	2.35	0.53	5.13	0.26	−0.21
	32.18	50.58	4.64	0.28	4.76	0.20	−0.36
C5−Br2	25.81	6.03	48.96	1.99	6.67	−0.42	−0.87
	32.13	4.72	51.07	0.58	4.72	−0.55	−0.84
Br2···Br3	−0.85	1.22	45.50	49.70	0.46	−1.66	−0.74
	0.83	3.18	36.80	49.02	0.87	−4.95	−2.72
Br2···H7	−19.81	15.04	7.07	15.63	15.20	−54.47	4.26
	−15.07	16.98	8.19	6.77	15.77	−86.06	3.34
Br2···H13	−21.38	17.94	9.23	13.44	4.15	−9.84	−40.37
	−35.58	26.30	2.85	7.32	10.41	−17.76	−80.37
S1···H13	−1.85	14.47	7.08	5.11	−8.58	−2.73	−41.43
	−12.23	18.15	14.94	2.98	−14.24	−4.93	−75.85

[†]Models: ZORA-BLYP-D3(BJ)/TZP//ZORA-M06-2X/QZ4P (*model 1*, first row of each entry), exp-geom//XCW-B3LYP/6-31G(d,p) (*model 4*, second row of each entry).

Table 6

Bond orders of non-covalent interactions in complex **1**, calculated using two models† and three different methods.

Method	Br2···Br3	Br2···H7	Br2···H13	S1···H13
FBO[a]	1.202	0.036	0.031	0.047
	0.772	0.033	0.021	0.036
MBO[b]	0.566	0.016	0.038	0.030
	0.346	0.025	0.028	0.054
WBO[c]	1.025	0.035	0.032	0.053
	0.494	0.032	0.018	0.034

†Models: ZORA-BLYP-D3(BJ)/TZP//ZORA-M06-2X/QZ4P (*model 1*, first row of each entry), exp-geom//XCW-B3LYP/6-31G(d,p) (*model 4*, second row of each entry). [a]Fuzzy bond order. [b]Mayer bond order. [c]Wiberg bond order.

The Interacting Quantum Atoms approach (IQA) adopts the real space partition of the electron density giving by the QTAIM methodology to obtain intra- and inter-atomic energy contributions from the atomic basins (Popelier & Kosov, 2001; Blanco, Pendás & Francisco, 2005). As opposed to traditional energy decomposition analyses, like EDA-NOCV, it is not necessary to define ambiguous fragments or reference states to perform the calculations, since the atomic basins are already given by the underlying QTAIM approach. In this way, it is possible to decompose the interaction energy between two atomic basins A and B (which can represent either bonded or non-bonded atoms), E_{int}^{AB}, into a classical term, V_{cl}^{AB}, and an exchange-correlation term, V_{xc}^{AB}: $E_{\text{int}}^{AB} = V_{cl}^{AB} + V_{xc}^{AB}$. Here, V_{cl}^{AB} and V_{xc}^{AB} can be associated with the electrostatic and covalent contributions to the interaction energy, respectively, which can be either negative (stabilizing interaction) or positive (destabilizing interaction) (Tiana *et al.*, 2011). Table 7 collects both contributions to the interaction energy for several interactions in complex **1**, calculated using models 1 (theoretical geometry) and 4 (experimental geometry), with equivalent results for the other two models. Notwithstanding the classical term for both the Br2···Br3 and C5···Br3 interactions is positive, the exchange-correlation term is negative, and even quite large for the former interaction, leading to an overall stabilizing interaction both in the crystal and in gas phase. By adding the values in Table 7, the covalent contribution to the Br2···Br3 interaction can be estimated to be between 56% (solid state) and 80% (gas phase), which show an excellent agreement with the estimations made from the DI's collected in Table 3. In addition, it may be seen again that the Br2···Br3 interaction is not particularly weak, having an interaction energy of, respectively, −89.7 kcal mol^{-1} and −38.1 kcal mol^{-1}, almost as strong

as typical covalent bonds like C5−Br1, C5−Br2, and C5−S1. The C5−P1 bond is even much stronger due to the opposite charges of C5 and P1 (Q_{P1} is between +1.6 and +1.8 e; see Table 2 for charges of the other atoms), leading to a large stabilizing electrostatic contribution to this bond. On the contrary, both Br2···H7 and Br2···H13 interactions are much weaker, as expected, with interaction energies ranging between −3 and −4 kcal mol^{-1} (not shown in the table).

A complementary way to the QTAIM partitioning of the molecular electron density is given by the Electron Localization Function approach (ELF), which is a measure of the likelihood of finding a same-spin electron in the neighbourhood of a reference electron (Becke & Edgecombe, 1990). ELF provides a useful method for mapping the electron pair probability and it is usually considered a kind of visualization of VSEPR theory, since it shows a neat separation in shells between core and valence electrons, as well as clearly visualizes covalent bonds and lone pairs, among other features. Dimensionless ELF ($0 \leq \eta \leq 1$) of complex **1** is depicted in Fig. 5, where disynaptic valence basins, *V*(C,Br), *V*(C,C), and *V*(P,C), among others, corresponding respectively to C–Br, C–C, and P–C bonds, are shown, as well as monosynaptic basins located at carbonyl O atoms, *V*(O), the sulphur atom, *V*(S), and bromine atoms, *V*(Br), corresponding to their lone pairs (monosynaptic basins for hydrogen atoms, *V*(H), are also shown in Fig. 5). Despite the fact that no disynaptic valence basin between Br2 and Br3 atoms, *V*(Br2,Br3), is observed in Fig. 5, thus showing the relevant electrostatic contribution to this interaction, this is only due to the high value of η represented (0.80), which emphasizes pure covalent bonds and lone pairs (at η = 0.45, *V*(Br2,Br3) separates into *V*(Br2) and *V*(Br3)). Two-dimensional projections of ELF depicted in Fig. 6 show that electron pairs for the covalent C5–Br1 and C5–Br2 bonds are localized between the valence basins of the bonded atoms, as expected (and in the lone pairs of bromine atoms as well), where $\eta \approx 1$ (almost complete localization), but scarcely in the region between Br2 and Br3 atoms, where η is much smaller. In fact, while the η function shows maxima, approximately equal to 0.90, next to both C5–Br1 and C5–Br2 *bcps*, it has a minimum close to the Br2···Br3 *bcp* (see Fig. S3 in the Supporting Information). On the other hand, while $\eta \approx 0.20$ at the Br2···Br3 *bcp*, $\eta < 0.05$ at both Br2···H7 and Br2···H13 *bcps* (Fig. S3), which again illustrates the different nature of both kinds of interaction.

Table 7

IQA contributions (in kcal mol^{-1}) to the bonding interaction energy ($E_{\rm int}^{AB}$) for selected interactions of complex **1**, calculated using two models†.

Term	C5−Br1	C5−Br2	Br2···Br3	C5···Br3	C5−S1	C5−P1
V_{cl}^{AB}	7.76	−15.51	1.64	21.95	8.89	−402.34
	1.46	−13.46	1.49	32.54	−4.39	−334.43
V_{xc}^{AB}	−156.98	−101.36	−91.35	−5.76	−192.48	−129.17
	−149.73	−145.72	−39.61	−3.50	−185.35	−123.73

†Models: ZORA-BLYP-D3(BJ)/TZP//ZORA-M06-2X/QZ4P (*model 1*, first row of each entry), exp-geom//XCW-B3LYP/6-31G(d,p) (*model 4*, second row of each entry).

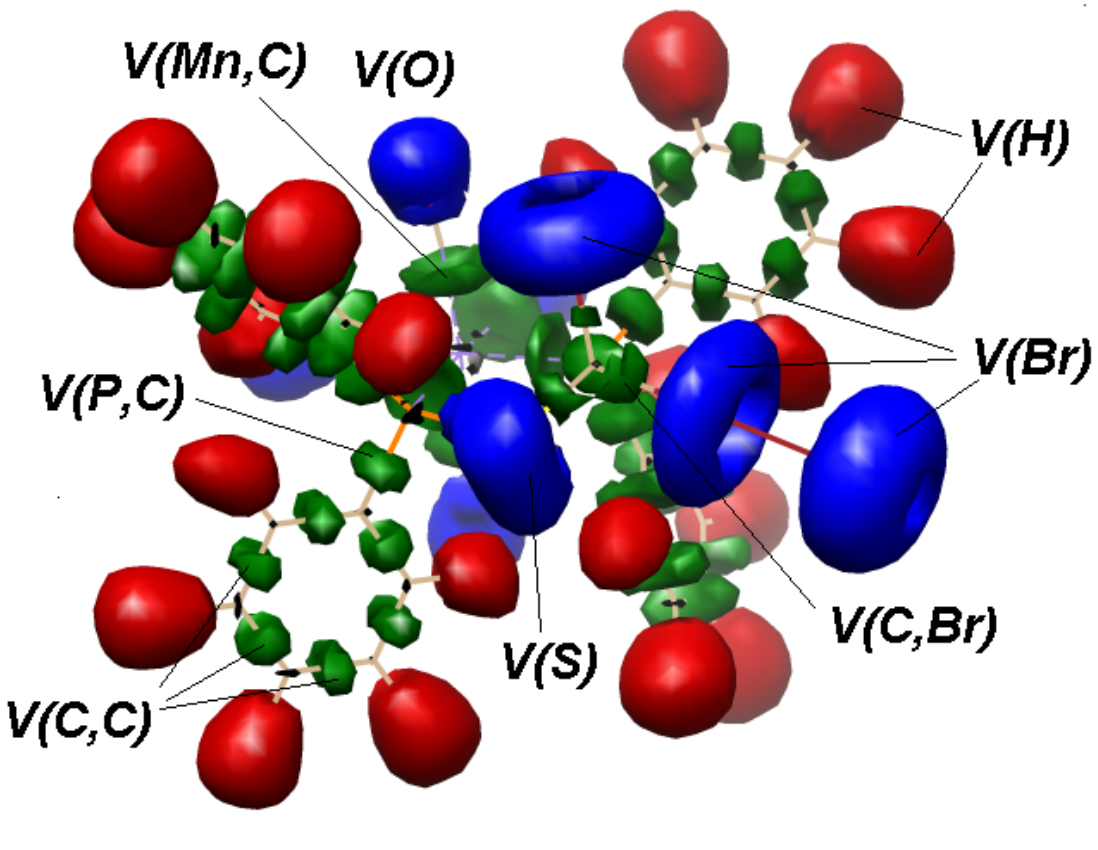

Figure 5

Electron localization function isosurface at η = 0.80 for complex **1** (model 4). Color codes: green for all disynaptic basins, black for all core basins, red for *V*(H), and blue for *V*(O), *V*(S), and *V*(Br).

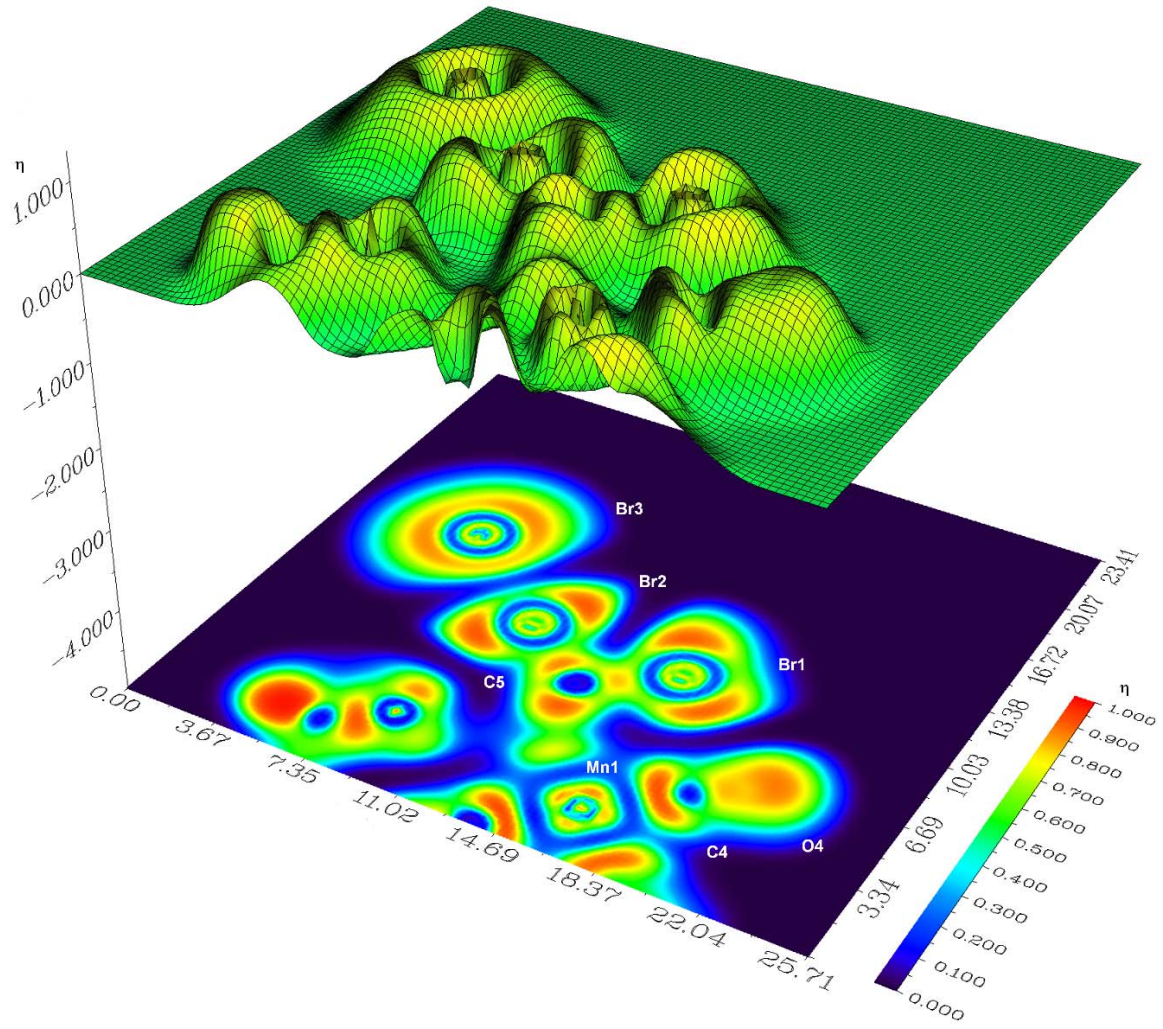

Figure 6

Electron localization function projection on the Br1–Br2–Br3 plane of complex **1** (distances in bohrs), calculated using model 4.

A closely related tool to ELF is the one-electron potential (OEP), $P(\boldsymbol{r})$, defined as (Hunter, 1986) $P(\boldsymbol{r}) = \frac{1}{4}\frac{\nabla^2\rho}{\rho} - \frac{1}{8}\frac{|\nabla\rho|^2}{\rho^2}$, where the second term is negative everywhere while the first term alternates with increasing $\boldsymbol{r}$. It has been recently shown that this function is particularly well suited for characterizing halogen bonds due to its clear physical meaning, even better than the Laplacian alone when heavy atoms are involved (Bartashevich *et al.*, 2017). Using model 4 (with equivalent results for model 3), in Fig. 7 the negative of OEP ($-P(\mathbf{r})$) is represented along the *bp* for the Br2···Br3 interaction, showing a negative minimum close to the *bcp*, surrounded by a positive maximum on the right, at the side of the Br3 atom, which acts as the electron donor in this pair of atoms, and a negative maximum at the side of the Br2 atom, which acts as the electron acceptor. This behaviour is not only

clearly different from the one shown by this function for both C5–Br1 and C5–Br2 covalent bonds (see Fig. S4 in the Supporting Information), where each one of the positive minima at its corresponding *bcp* is surrounded by two positive maxima, but also from the observed behaviour of $P(\boldsymbol{r})$ along *bps* for both Br2···H7 and Br2···H13 interactions. The subtle differences between C5–Br1 and C5–Br2 interactions may be better appreciated by using the Laplacian itself, which is depicted in Fig. 8 using models 1 (theoretical geometry) and 4 (experimental geometry), while profiles for the Laplacian along C5–Br1, C5–Br2, and Br2···Br3 *bps* are shown in Fig. S5. As may be seen in Fig. 8, the C5–Br2 *bcp* in the gas phase is located in the positive region of the Laplacian, whereas it is located in the negative region in the solid state, as previously mentioned (see Table 3). In addition, while in gas phase Laplacian´s own critical points for the C5–Br2 bond resemble those of the Br2···Br3 interaction more than those of the C5–Br1 interaction, the opposite holds in the solid state. Therefore, in gas phase the C5–Br2 interaction is closer to a halogen bond than to a typical covalent bond between different non-metal atoms. On the other hand, for the Br2···Br3 interaction the Laplacian shows large similarities between the gas phase and the solid state (see Figure 8), as already shown in the data collected in Table 3.

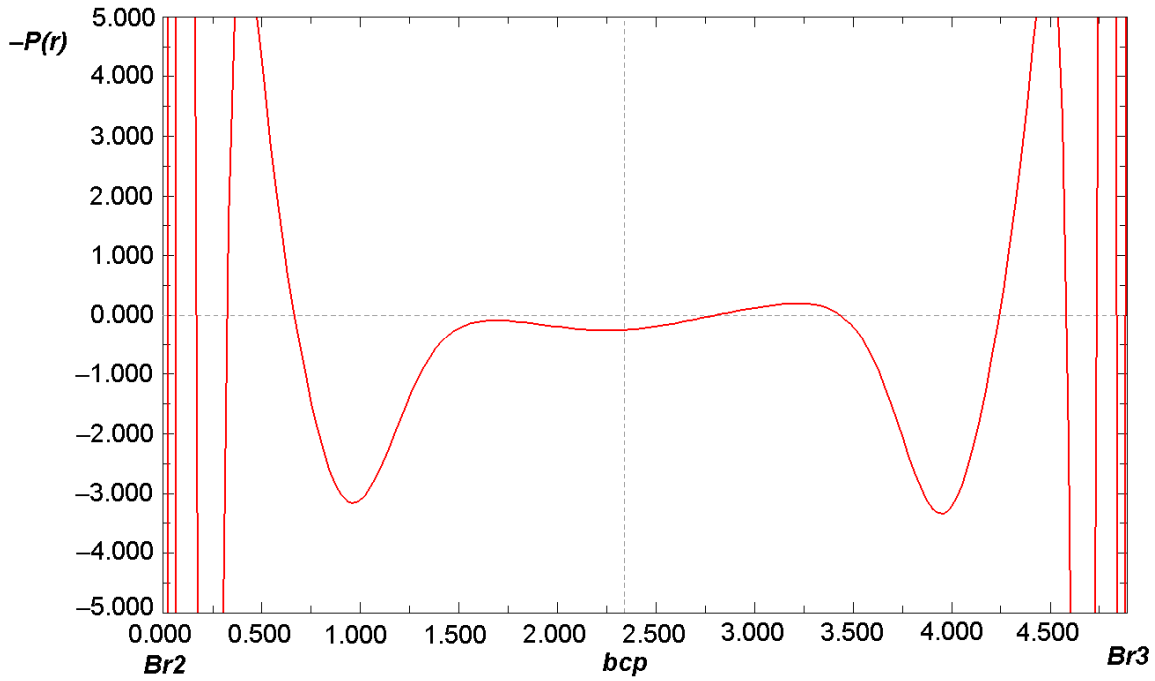

Figure 7

Negative one-electron potential (in a.u.) along the Br2···Br3 bond path of complex **1**. The location of the bond critical point is shown by a dotted vertical line (distances in bohrs).

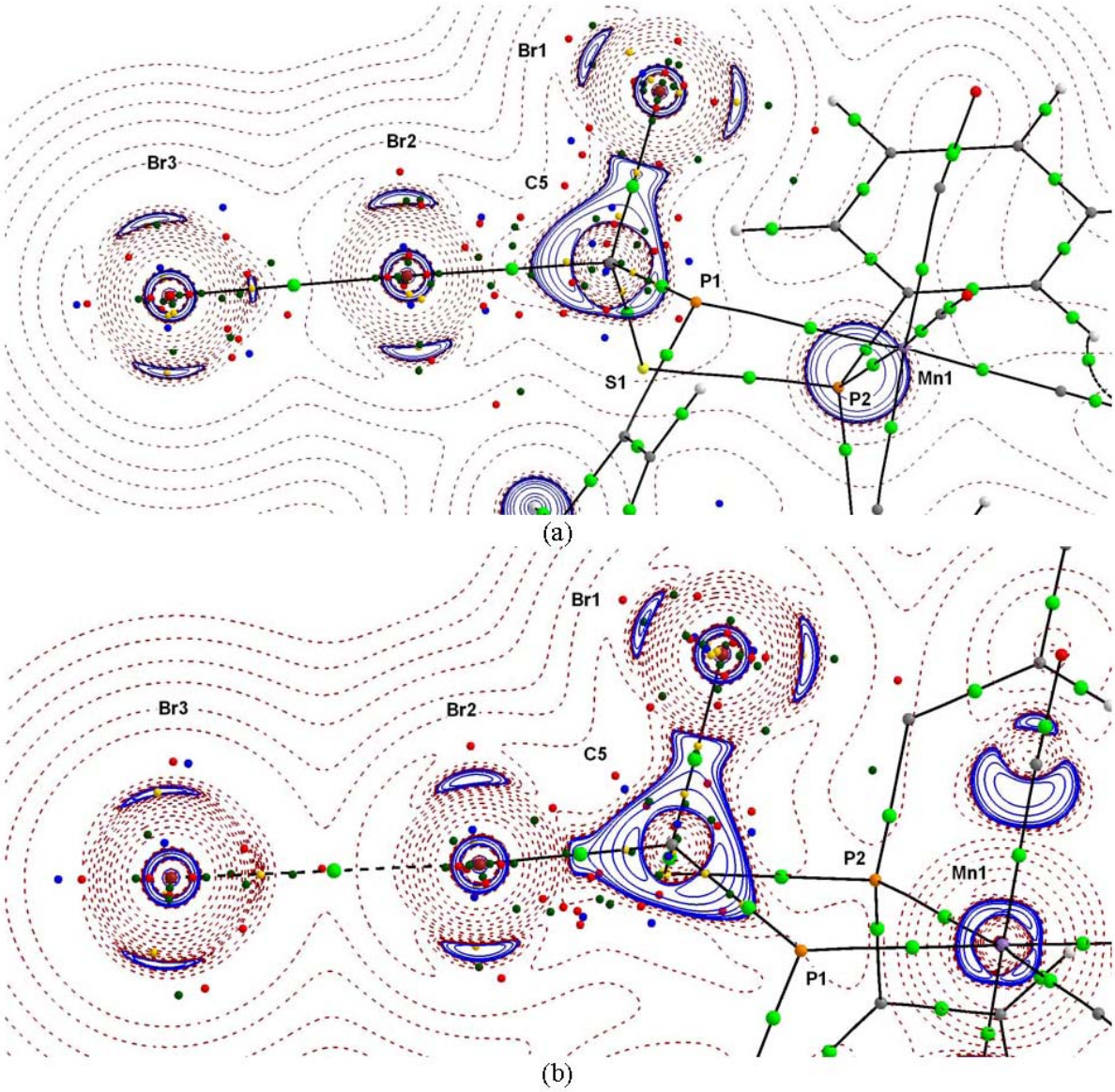

Figure 8

Laplacian of the electron density on the Br1–Br2–Br3 plane of complex **1** (contour levels at 0.0 and ±(1,2,4,8)×10^n e $Å^{-5}$, with n ranging from +3 to –3), using: (a) model 1 (theoretical geometry), and (b) model 4 (experimental geometry). Blue and red lines represent negative and positive values, respectively. Colour codes: light green for *bcps*, and yellow, dark green, red, and blue for, respectively, (3,+3), (3,+1), (3, –1), and (3, –3) Laplacian´s critical points.

One further tool that can be used to characterize non-covalent interactions like the ones observed in complex **1** is the Reduced Density Gradient method (RDG), which is particularly useful for the analysis of weak interactions by means of a type of non-covalent interaction index (NCI) (Johnson *et al.*, 2010). To distinguish weak interaction regions from other regions in the molecule, the RDG

method uses the dimensionless reduced electron density gradient NCI index, $s = \frac{1}{2(3\pi^2)^{\frac{1}{3}}} \frac{|\nabla\rho|}{\rho^{\frac{4}{3}}}$, which discriminates weak interactions (small ρ, very small $\nabla\rho$, medium s) from the rest of interactions in the molecule. Using model 4, in Fig. 9a the s index of complex **1** is plotted against sign(λ_2)ρ, where λ_2 is the second highest eigenvalue of the electron density's Hessian matrix. The few spikes at the bottom of the plot, which point towards low values of ρ, reveal the existence of non-covalent interactions in **1**, both attractive (negative λ_2) and repulsive (positive λ_2). By taking the value s = 0.25 (horizontal line in Fig. 9a), the isosurface depicted in Fig. 9b shows only the weak interactions and, at the same time, can beautifully discriminate between different types of non-covalent interactions. The strongest attractive one is that corresponding to the Br2···Br3 bonding interaction (λ_2 negative and $\rho \approx 0.025$ au, see Figure 9a and Table 3), while the smallest attractive ones (λ_2 negative and ρ around 0.010 au) refer to Br2···H7, Br2···H13, and S1···H13 interactions. The repulsive interactions (λ_2 positive) refer mainly to steric effects inside phenyl rings.

Finally, in order to further quantify energetically the non-covalent interactions observed in **1**, a Natural Bond Orbital (NBO) analysis has also been performed (Weinhold & Landis, 2012). The overlap between one of the Br3 lone pairs and an empty σ MO of the C5–Br2 bond, responsible of the charge transfer between them ($n_{Br3} \rightarrow \sigma^*$(C5–Br2)) and calculated using model 3 (with equivalent results for the other models) is represented in Fig.10. The stabilizing energy obtained from the second order perturbation theory applied to the interaction involving a lone pair of the donor (Br3) and an empty antibonding σ orbital of the acceptor (C5–Br2) ranges between 23.23 and 27.16 kcal mol^{-1}, depending on the model used (with the highest electron donation occurring in the gas phase), which is notably higher than the values between 0.59 and 1.21 kcal mol^{-1}, calculated for the $n_{S1} \rightarrow \sigma^*$(C13–H13) interaction, not to mention values less than 0.50 kcal mol^{-1} for both $n_{Br2} \rightarrow \sigma^*$(C7–H7) and $n_{Br2} \rightarrow \sigma^*$(C13–H13) interactions. By means of a comparison, for the weak Br···Br interactions in {(2-BrPy)$_2$H}[BiBr$_4$] and 2-(BrPyH)$_2$[BiBr$_5$],which are dominated by electrostatics, the stabilizing energy is only 0.9 and 5.6 kcal mol^{-1} respectively (Adonin *et al.*, 2017).

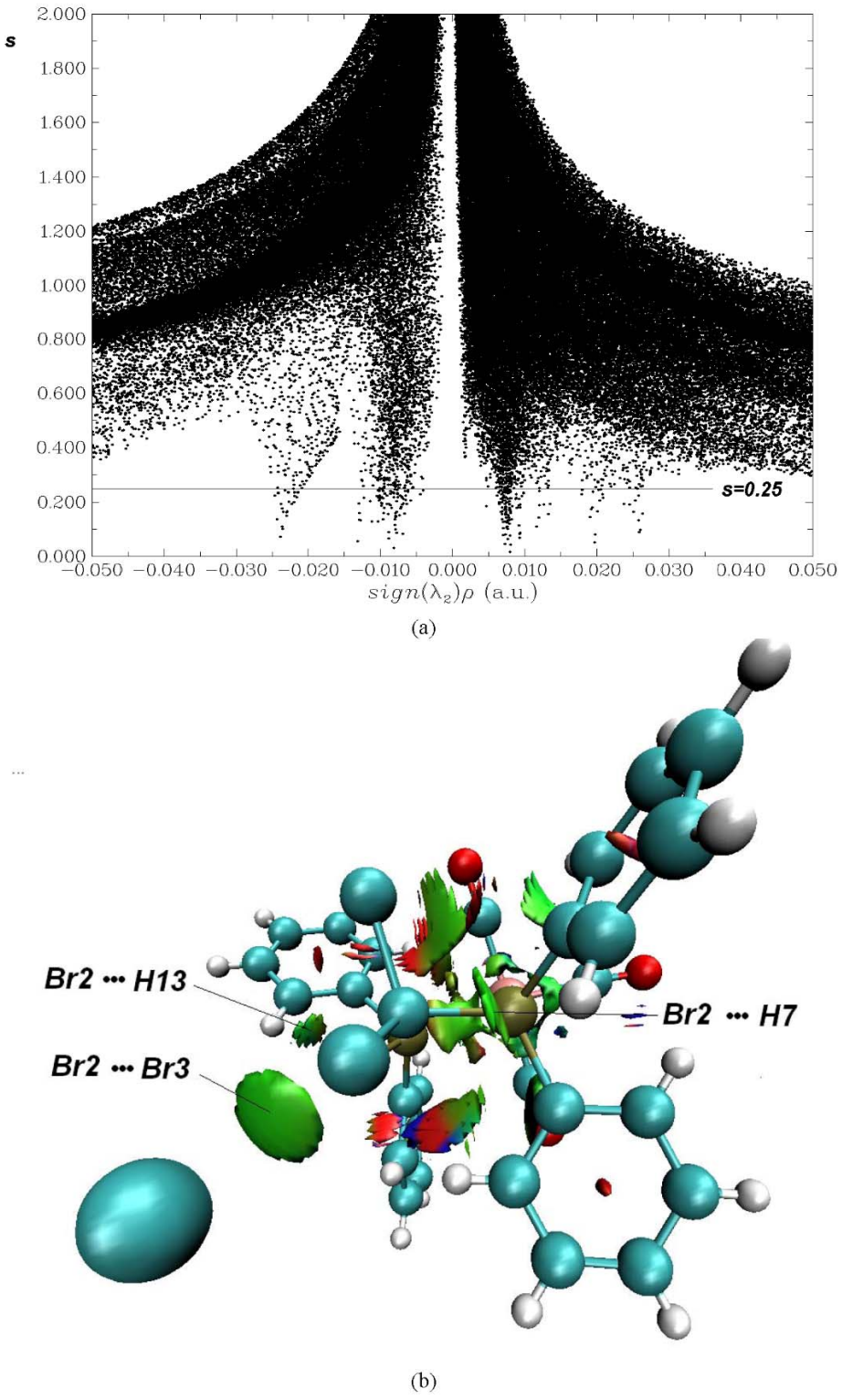

Figure 9

(a) Reduced Density Gradient (*s* function) plotted vs. sign(λ_2)ρ (au) for **1**. (b) RDG isosurfaces (*s* = 0.25) for **1**. Colour code: green (relatively strong attraction: $\rho > 0$, $\lambda_2 < 0$), blue (very small attraction or repulsion: ρ close to 0, λ_2 close to 0), red (relatively strong repulsion: $\rho > 0$, $\lambda_2 > 0$).

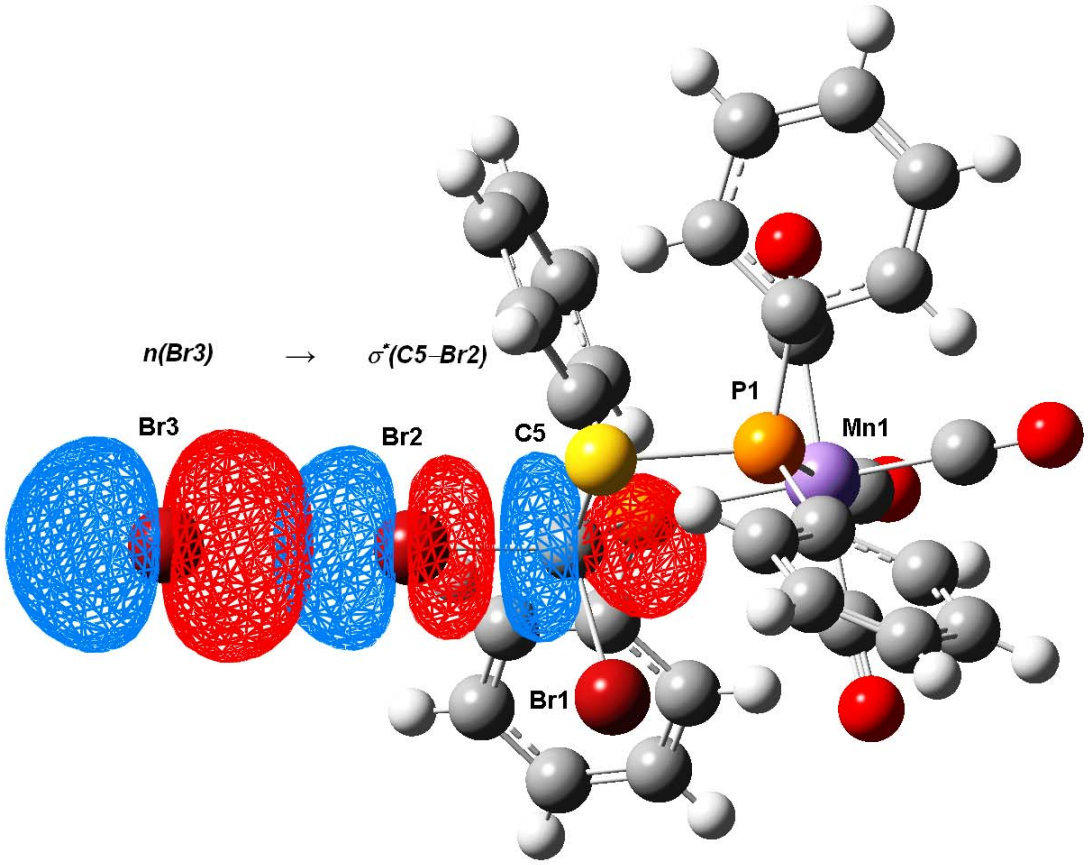

Figure 10

NBO representation of the overlap between a lone pair of the Br3 atom and an empty σ MO of the C5–Br2 bond.

4. Conclusions

Synthesis, structure characterization, and bonding in the carbonyl complex $[Mn(CO)_4\{(C_6H_5)_2P–S–C(Br_2)–P(C_6H_5)_2\}]Br$ (**1**) have been described in the current work. The synthesis of complex **1** is itself highly remarkable, as it implies an unprecedented insertion reaction of a sulphur atom into a strong P–C bond. To the best of our knowledge, this is the first example of such an insertion. The structure of **1**, showing a P–C–S–P expanded skeleton for the diphosphine ligand is also unique. Bonding has been analysed using the Quantum Theory of Atoms in Molecules (QTAIM), the Electron Localization Function (ELF), and the Natural Bond Orbital (NBO) approaches applied to both the experimental geometry (solid state) and the theoretically optimized geometry (gas phase), through the calculation of several tools related to bond order, bond strength, and covalent/electrostatic character of bonds, like the Electrostatic Potential (ESP), the Reduced Density Gradient (RDG), the Source

Function (SF), the interaction energies based on the Interacting Quantum Atoms approach (IQA), and the One-Electron Potential (OEP), among others. The main conclusions obtained from the current study are as follows.

(1) The two C–H···Br–C interactions found in **1** are of mainly electrostatic nature and can be safely labelled as weak hydrogen bonds.

(2) The covalent contribution to the C–Br···Br interaction in **1** has been estimated to be between 50% in the solid state and 80% in gas phase, with a highly stabilizing charge transfer from a lone pair of the terminal Br atom to a σ antibonding orbital of the C–Br covalent bond. As a consequence of the higher electron donation occurring in the gas phase: (a) the terminal Br atom (Br3) in the solid state is more negatively charged (−0.76 e) than in the gas phase (−0.49 e), thus having a more Br^--like behaviour in the solid state; (b) the C5–Br2 bond is clearly longer (0.2 Å) than the C5–Br1 bond in the gas phase, while they have almost the same bond distance in the solid state; and (c) the dihalogen C–Br···Br interaction observed in **1** can be labelled as a polar-covalent bond.

(3) The two C–Br interactions present in **1**, which are of almost identical nature in the solid state, show significant differences in gas phase, with one of them (Br1) remaining as pure covalent while the other (Br2, which involves the Br atom also participating in the above dihalogen bond and two hydrogen bonds) evolving into a halogen bond itself with many similarities with the Br···Br interaction. In particular, the C5–Br2 Laplacian distributions are clearly different in the gas phase and in the solid state, while they are almost identical for the C5–Br1 bond. This result is again a consequence of the differences in the $n_{Br3} \rightarrow \sigma^*$(C5–Br2) charge transfer between the solid state and the gas phase.

(4) Although complex **1** is completely ionized in solution (consisting of solvated Br^- and $[Mn(CO)_4\{(C_6H_5)_2P–S–C(Br_2)–P(C_6H_5)_2\}]^+$ ions), both in gas phase and in the solid state a directional Br···Br interaction with a high degree of covalency has been observed.

5. Related literature

References cited in the supporting information include: Altomare *et al.* (1999), Blessing (1987, 1989), Bruker (2006), Farrugia (2012), Sheldrick (2015), Sheldrick & Van der Maelen (1996), Siemens (1995), Spek (2009), and Van der Maelen (1999).

Acknowledgements The authors declare no financial interest. The authors would also like to thank the referees for their valuable contributions.

References

Adonin, S. A., Gorokh, I. D., Novikov, A. S., Abramov, P. A., Sokolov, M. N. & Fedin, V. P. (2017). *Chem. Eur. J.* **23**, 15612-15616.

Altomare, A., Burla, M. C., Camalli, M., Cascarano, G. L., Giacovazzo, C., Guagliardi, A., Moliterni, A. G. G., Polidori, G. & Spagna, R. (1999). *J. Appl. Cryst.* **32**, 115–119.

Bader, R. F. W. (1990). *Atoms in Molecules: A Quantum Theory*. Oxford: Clarendon Press, 1990.

Baerends, E. J. *et al.* (2012). ADF2012, revision 01d, SCM, Theoretical Chemistry, Vrije Universiteit: Amsterdam, The Netherlands.

Bartashevich, E., Yushina, I., Kropotina, K., Muhitdinova, S. & Tsirelson, V. (2017). *Acta Cryst.* B**73**, 217-226.

Bartashevich, E., Muhitdinova, S., Yushina, I., & Tsirelson, V. (2019). *Acta Cryst.* B**75**, 117-126.

Becke, A. D. & Edgecombe, K. E. (1990). *J. Chem. Phys.* **92**, 5397-5403.

Biegler-Kӧnig, F. & Schӧnbohm, J. (2002). *J. Comput. Chem.* **23**, 1489−1494.

Blanco, M. A., Pendás, A. M. & Francisco, E. (2005). *J. Chem. Theory Comput.* **1**, 1096–1109.

Blessing, R. (1987). *Cryst. Rev.* **1**, 3–58.

Blessing, R. (1989). *J. Appl.Cryst.* **22**, 396–397.

Brugos, J., Cabeza, J. A., García-Álvarez, P., Kennedy, A. R., Pérez-Carreño, E. & Van der Maelen, J. F. (2016). *Inorg. Chem.* **55**, 8905−8912.

Brugos, J., Cabeza, J. A., García-Álvarez, P., Pérez-Carreño, E. & Van der Maelen, J. F. (2017). *Dalton Ttrans.* **46**, 4009–4017.

Bruker (2006). APEX2, Version 2 User Manual, M86-E01078, Bruker Analytical X-ray Systems, Madison, Wisconsin, USA.

Bytheway, I., Grimwood, D. J., Figgis, B. N., Chandler, G. S. & Jayatilaka, D. (2002). *Acta Cryst.* A**58**, 244-251.

Bučinský, L., Jayatilaka, D. & Grabowsky, S. (2016). *J. Phys. Chem. A*, **120**, 6650-6669.

Cabeza, J. A., Fernández-Colinas, J. M., García-Álvarez, P., Pérez-Carreño, E., Pruneda, V. & Van der Maelen, J. F. (2013). *Chem. - Eur. J.* **19**, 9251−9260.

Cabeza, J. A., Van der Maelen, J. F. & García-Granda, S. (2009). *Organometallics* **28**, 3666−3672.

Cavallo, G., Metrangolo, P., Milani, R., Pilati, T., Priimagi, A., Resnati, G. & Terraneo, G. (2016). *Chem. Rev.* **116**, 2478-2601.

Clark, T., Hennemann, M., Murray, J. S. & Politzer, P. (2007). *J. Mol. Model.* **13**, 291-296.

Colin, J. J. (1814). *Ann. Chim.* **91**, 252-272.

Coppens, P. (1997). *X-ray Charge Densities and Chemical Bonding*. Oxford University Press.

Desiraju, G. R., Ho, P. S., Kloo, L., Legon, A. C., Marquardt, R., Metrangolo, P., Politzer, P., Resnati, G. & Rissanen, K. (2013). *Pure Appl. Chem.* **85**, 1711-1713.

Dittrich, B., Sze, E., Holstein, J. J., Hübschle, C. B. & Jayatilaka, D. (2012). *Acta Cryst.* A**68**, 435-442.

Erdelyi, M. & Metrangolo, P. (2017). *Acta Cryst.* B**73**, 135.

Espinosa, E., Alkorta, I., Elguero, J. & Molins, E. (2002). *J. Chem. Phys.* **117**, 5529-5542.

Farrugia, L. J. (2012). *J. Appl. Cryst.* **45**, 849-854.

Frenking, G. & Shaik, S., Eds. (2014). *The Chemical Bond*. Weinheim (Germany): Wiley-VCH.

Frisch, M. J. *et al.* (2009). Gaussian09, revision B.01, Gaussian Inc., Wallingford, CT, USA.

Gatti, C. (2005). *Z. Kristallogr. - Cryst. Mater.* **220**, 399−457.

Gatti, C.; Lasi, D. (2007). *Faraday Discuss.* **135**, 55−78.

Gatti, C. & Macchi, P., Eds. (2012). *Modern Charge Density Analysis*. Heidelberg (Germany): Springer.

Gilday, L. C., Robinson, S. W., Barendt, T. A., Langton, M. J., Mullaney, B. R. & Beer, P. D. (2015). *Chem. Rev.* **115**, 7118-7195.

Glendening, E. D., Badenhoop, J. K., Reed, A. E., Carpenter, J. E., Bohmann, J. A., Morales, C. M., Karafiloglou, P., Landis, C. R. & Weinhold, F. (2018). NBO 7.0. Theoretical Chemistry Institute, University of Wisconsin, Madison (WI, USA).

Grabowsky, S. J. (2011). *Chem. Rev.* **111**, 2597-2625.

Grabowsky, S. J. (2018). *Intermolecular Interactions in Crystals: Fundamentals of Crystal Engineering*, edited by J. J. Novoa, pp. 478-515. London: The Royal Society of Chemistry.

Grabowsky, S. J. (2020). *Coord. Chem. Rev.* **407**, 213171.

Grabowsky, S. J., Luger, P., Buschmann, J., Schneider, T., Schirmeister, T., Sobolev, A. N. & Jayatilaka, D. (2012). *Angew. Chem. Int. Ed.* **51**, 6776-6779.

Grimme, S., Ehrlich, S. & Goerigk, L. (2011). *J. Comput. Chem.* **32**, 1456-1465.

Grimwood, D. J. & Jayatilaka, D. (2001). *Acta Cryst.* A**57**, 87-100.

Hansen, N. K. & Coppens, P. (1978). *Acta Cryst.* A**34**, 909-921.

Hunter, G. (1986). *Int. J. Quantum Chem.* **29**, 197-204.

Jayatilaka, D & Dittrich, B. (2008). *Acta Cryst* A**64**, 383-393.

Jayatilaka, D. & Grimwood, D. J. (2001). *Acta Cryst.* A**57**, 76-86.

Jayatilaka, D. & Grimwood, D. J. (2003). In *Computational Science – ICCS 2003, Lecture Notes in Computer Science*, Vol 2660, edited by P. M. A. Sloot *et al.*, pp. 142-151, Springer, Melbourne, Australia.

Jelsch, C. & Guillot, B. (2017). *Acta Cryst.* B**73**, 136-137.

Johnson, E. R., Keinan, S., Mori-Sánchez, P., Contreras-García, J., Cohen, A. J. & Yang, W. (2010). *J. Am. Chem. Soc.* **132**, 6498–6506.

Keith, T. A. (2015). AIMAll, version 15.09.27, TK Gristmill Software, Overland Park, KS, USA.

Kohout, M. (2011). DGrid-4.6, Max Planck Institute for Physical Chemistry of Solids, Dresden, Germany.

Lu, T. & Chen, F. (2012). *J. Comput. Chem.* **33**, 580−592.

Macchi, P. (2013). *Cryst. Rev.* **19**, 58–101.

Martínez-Amezaga, N. J., Pamies, S. C., Peruchena, N. M. & Sosa, G. L. (2010). *J. Phys. Chem. A*, **114**, 552-562.

Matta, C. F. & Boyd, R. J., Eds. (2007). *The Quantum Theory of Atoms in Molecules*. Weinheim (Germany): Wiley-VCH.

Mayer, I. (2016). *Bond Orders and Energy Components: Extracting Chemical Information from Molecular Wave Functions*. Boca Ratón, FL, USA: CRC Press.

Mayer, I. & Salvador, P. (2004). *Chem. Phys. Lett.* **383**, 368-375.

Metrangolo, P., Meyer, F., Pilati, T., Resnati, G. & Terraneo, G. (2008). *Angew. Chem. Int. Ed.* **47**, 6114-6127.

Pettersen, E. F., Goddard, T. D., Huang, C. C., Couch, G. S., Greenblatt, D. M., Meng, E. C. & Ferrin, T. E. (2004). *J. Comput. Chem.* **25**, 1605−1612.

Politzer, P., Murray, J. S. & Clark, T. (2010). *Phys. Chem. Chem. Phys.* **12**, 7748-7757.

Popelier, P. L. A. (2000). *Atoms in Molecules: An Introduction*, Upple Saddle River (NJ, USA): Prentice Hall.

Popelier, P. L. A. & Kosov, D. S. (2001). *J. Chem. Phys.* **114**, 6539–6547.

Rowe, R. K. & Ho, P. S. (2017). *Acta Cryst.* B**73**, 255-264.

Ruiz, J., Ceroni, M., Quinzani, O. V., Riera, V., Vivanco, M., García-Granda, S., Van der Maelen, J. F., Lanfranchi, M. & Tiripicchio, A. (2001). *Chem. Eur. J.* **7**, 4422-4430.

Ruiz, J., Quesada, R., Vivanco, M., García-Granda, S. & Díaz, M. R. (2007). *Organometallics* **26**, 1703-1711.

Ruiz, J., Sol, D., García, L., Mateo, M. A., Vivanco, M. & Van der Maelen, J. F. (2019). *Organometallics* **38**, 916-925.

Schiffer, M. & Scheer, M. *Angew. Chem. Int. Ed.* **2001**, *40*, 3413-3416.

Shahbazian, S. (2018). *Chem. Eur. J.* **24**, 5401-5405.

Sheldrick, G. M. (2015). *Acta Cryst.* C**71**, 3-8.

Sheldrick, G. M. & Van der Maelen, J. F. (1996). *Anal. Quim. Int. Ed.* **92**, 7-12.

Siemens (1995). SMART System, Siemens Analytical X-ray Instruments, Madison, USA.

Spek, A. L. (2009). *Acta. Cryst.* D**65**, 148-155.

Streubel, R., Wilkens, H. & Jones, P. G. (2000). *Chem. Eur. J.* **6**, 3997-4000.

Tiana, D., Francisco, E., Blanco, M. A., Macchi, P., Sironi, A.& Pendás, A. M. (2011). *Phys. Chem. Chem. Phys.* **13**, 5068–5077.

Thirman, J., Engelage, E., Huber, S.M. & Head-Gordon, M. (2018). *Phys. Chem. Chem. Phys.* **20**, 905-915.

Van der Maelen, J. F. (1999). *Cryst. Rev.* **7**, 125–187.

Van der Maelen, J. F. (2020). *Organometallics* **39**, 132–141.

Van der Maelen, J. F., Brugos, J., García-Álvarez, P. & Cabeza, J. A. (2020). *J. Mol. Struct.* **1201**, 127217.

Van der Maelen, J. F. & Cabeza, J. A. (2012). *Inorg. Chem.* **51**, 7384−7391.

Van der Maelen, J. F. & Cabeza, J. A. (2016). *Theor. Chem. Acc.* **135**, 64.

Van der Maelen, J.F. & García-Granda, S. (2015). *AIP Conf. Proc.* **1642**, 563-566.

Van der Maelen, J. F., García-Granda, S. & Cabeza, J. A. (2011). *Comput. Theor. Chem.* **968**, 55−63.

Van der Maelen, J. F., Gutiérrez-Puebla, E., Monge, A., García-Granda, S., Resa, I., Carmona, E., Fernández-Díaz, M. T., McIntyre, G. J., Pattison, P. & Weber, H.-P. (2007). *Acta Cryst.* B**63**, 862-868.

Wang, H., Wang, W. & Jin, W. J. (2016). *Chem. Rev.* **116**, 5072-5104.

Weinhold, F. & Landis, C. R. (2012). *Discovering Chemistry with Natural Bond Orbitals*. New York: Wiley.

Wiberg, K. B. (1968). *Tetrahedron* **24**, 1083-1096.

Woińska, M., Jayatilaka, D., Spackman, M. A., Edwards, A. J., Dominiak, P. M., Woźniak, K., Nishibori, E., Sugimoto, K. & Grabowsky, S. J. (2014). *Acta Cryst.* A**70**, 483-498.

Woińska, M., Jayatilaka, D., Dittrich, B., Flaig, R., Luger, P., Woźniak, K., Dominiak, P. M. & Grabowsky, S. (2014). *ChemPhysChem*, **18**, 3334-3351.

Woińska, M., Wanat, M., Taciak, P., Pawinski, T., Minor, W. & Woźniak, K. (2019). *IUCr J.* **6**, 868-883.

Yamamoto, Y. & Sugawara, K. (2000). *Dalton Trans.* 2896-2897.

Zhao, Y. & Truhlar, D. G. (2008). *Theor. Chem. Acc.* **120**, 215-241.

Supporting information

S1. Synthesis and crystallization of $[Mn(CO)_4(P(C_6H_5)_2)_2SCBr_2]Br$

To a solution of the complex $[(CO)_4Mn\{(Ph_2P)_2C\text{-}S_2\text{-}C(PPh_2)_2\}Mn(CO)_4]$ (30 mg, 0.026 mmol) in CH_2Cl_2 (5 mL), a solution of Br_2 in CH_2Cl_2 (5.3 mL, 0.1 M, 0.53 mmol) was added under continuous stirring. The resulting mixture was stirred for 0.5 h. The solution was then filtered and the solvent eliminated to dryness under vacuum. The residue was washed with diethyl ether (3 x 5 mL) to yield a yellow solid. Yield: 27 mg (63 %).

Crystals suitable for an X-ray study were obtained by slow diffusion of hexane into a dichloromethane solution of the compound, although most of the crystals obtained were twinned and then discarded for the X-ray study.

S2. Spectroscopic data of $[Mn(CO)_4(P(C_6H_5)_2)_2SCBr_2]Br$

IR (CH_2Cl_2, cm^{-1}, ν(CO)): 2103 (s), 2041 (s), 2029 (vs), 2020 (sh).

$^{31}P\{^1H\}$ NMR (CD_2Cl_2): δ 113.2 (br, PSC), 137.1 (br, $PCBr_2$).

S3. X-ray structure determination of $[Mn(CO)_4(P(C_6H_5)_2)_2SCBr_2]Br$

A yellow crystal, 0.264 × 0.231 × 0.099 mm size, was used for collecting data in a Bruker APEX-II CCD single crystal diffractometer provided with a MoK_α radiation graphite crystal monochromator (λ = 0.71073 Å). Measurements were made both at room temperature and at 100 K, but the latter were discarded for this study due to the twinning observed. Unit cell dimensions were determined using Bruker software (Bruker, 2006). Space group C2 was found from systematic absences and structure determination. 3749 reflections were measured, hkl range (-18, 0, -17) to (18, 19, 0), theta limits ($1.42° < \theta < 25.97°$). SAINT v8.34A (Siemens, 1995) integration software was used for cell refinement and SORTAV (Blessing, 1987, 1989) was used for data reduction. A semi-empirical absorption correction was applied using a multi-scan technique (minimum and maximum transmission factors, respectively, 0.528 and 0.996).

The structure was solved by direct methods using the program SIR-97 (Altomare *et al.*, 1999). Isotropic least-squares refinement, using the program SHELXL-2018/3 (Sheldrick, 2015), converged to R = 0.077. A subsequent full matrix anisotropic least-squares refinement over F^2, using the same software, followed by a Difference Fourier synthesis allowed the location of some of the hydrogen atoms. Positional parameters and anisotropic displacement parameters of the non-hydrogen atoms were then refined. Hydrogen atoms were geometrically fixed to their parent atoms and isotropically

refined with their displacement parameters constrained to be $1.2U_{eq}$ of their parent atoms in order to increase the reflexions/parameters ratio. A rather disordered solvent area containing several molecules of CH_2Cl_2 could not be modelled by means of any constrained/restrained method, and thus it was treated by the SQUEEZE procedure included in the PLATON program package (Spek, 2009) (further details about refinement protocols may be found elsewhere: Van der Maelen & Sheldrick, 1996; Van der Maelen, 1999).

Final conventional agreement factors were R(F) = 0.046 for the 2399 'observed' reflections and 361 variables, and wR(F2) = 0.127 for the whole set of 3603 reflections. The function minimized was $w(|Fo|^2-|Fc|^2)^2$, $w = 1/(\sigma^2(Fo^2) + (0.0823P)^2)$, with $\sigma(Fo)$ obtained from counting statistics and $P = (Fo^2 + 2Fc^2)/3$. The maximum shift over error ratio in the last full matrix least-squares cycle was less than 0.001, while the final Difference Fourier map showed no peaks higher than 0.68 e/Å^3 nor deeper than -0.50 e/Å^3. The residual density map is shown in Fig. S2 (note that the highest residuals are positioned close to Br atoms, where their lone pairs are located). Atomic scattering factors were taken from the International Tables for Crystallography (1995). CIF files and other publication material created with the aid of WinGX (Farrugia, 2012).

Figure S1

IR spectrum of $[Mn(CO)_4(P(C_6H_5)_2)_2SCBr_2]Br$.

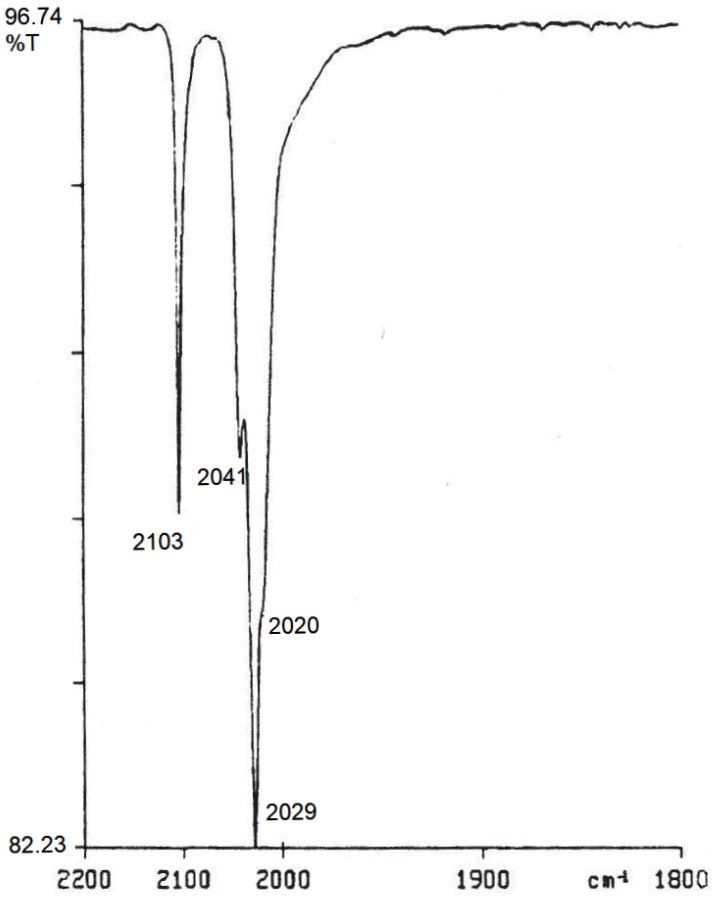

Figure S2

Residual electron density map from the X-ray refinement. The contour intervals are drawn at ±0.10 e Å^{-3} (dotted red lines: negative values, full green lines: positive values, dotted blue lines: zero value).

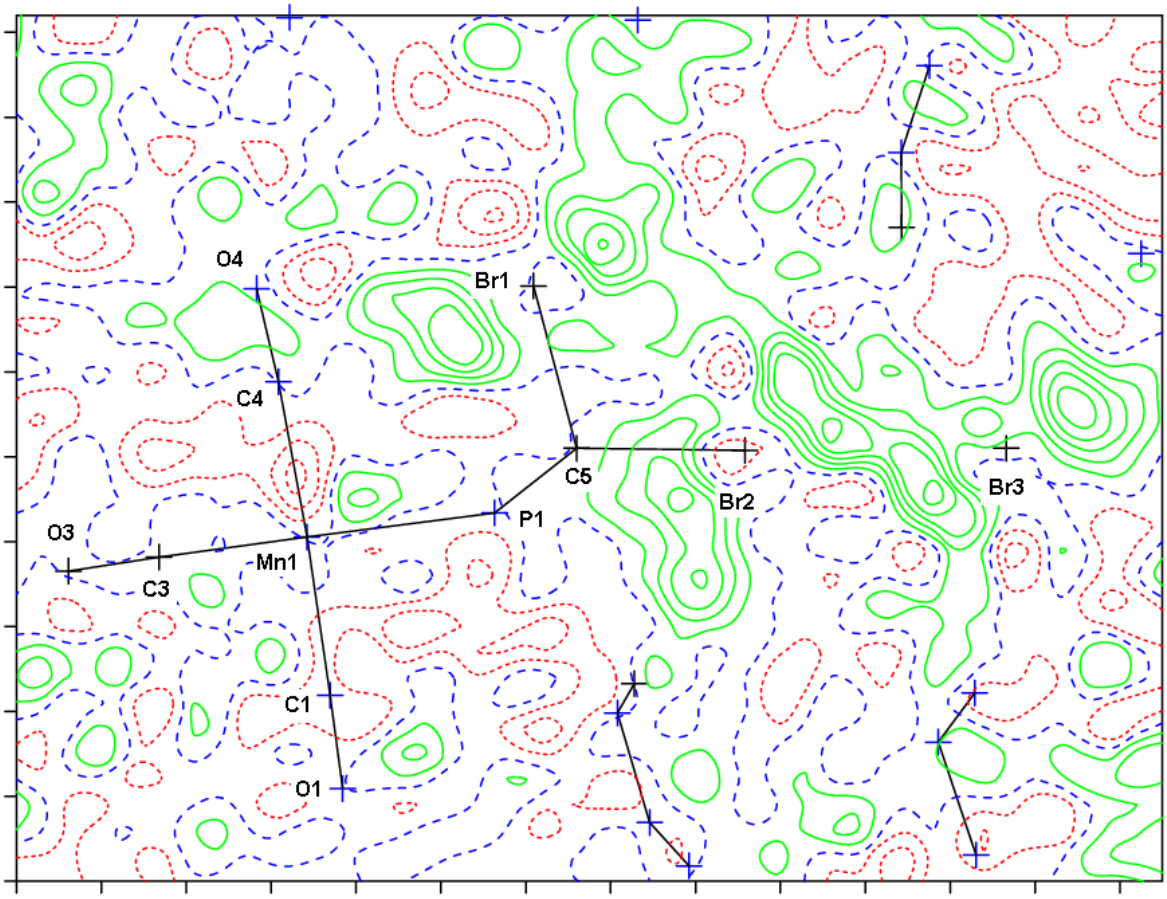

Figure S3

ELF along several bond paths of complex **1**. The location of bond critical points is shown by a dotted vertical line (distances in bohrs): (a) C5–Br1, (b) C5–Br2, (c) Br2···Br3, (d) Br2···H7, and (e) Br2···H13.

(a)

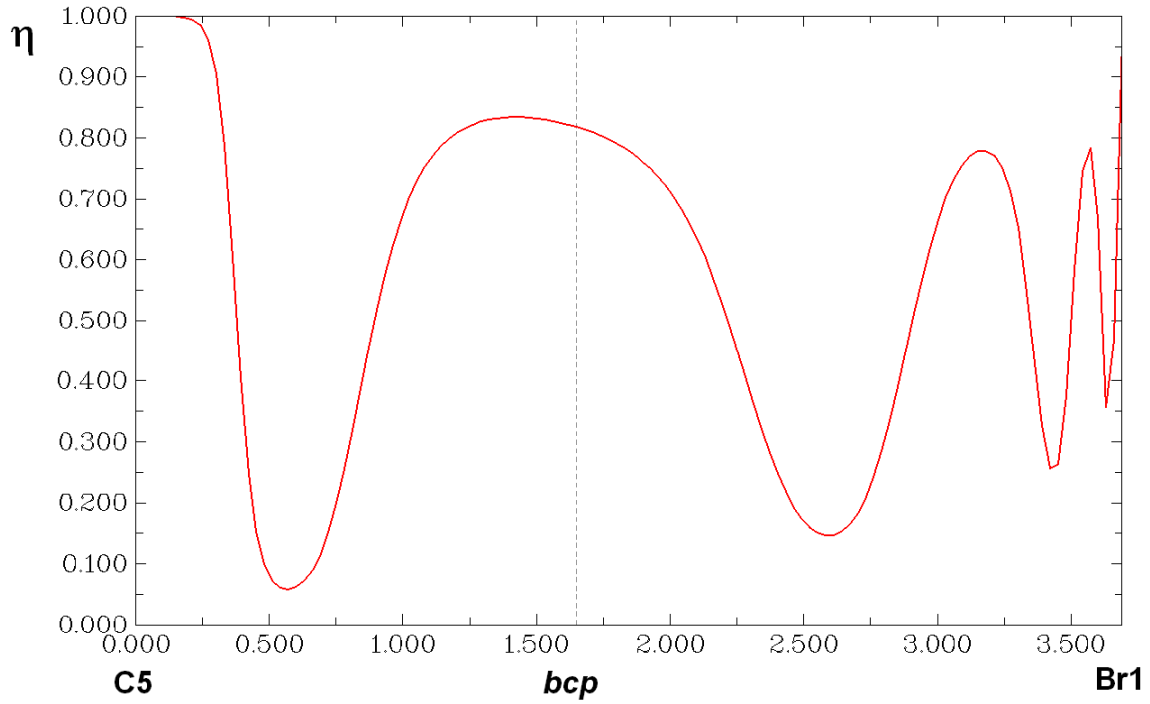

(b)

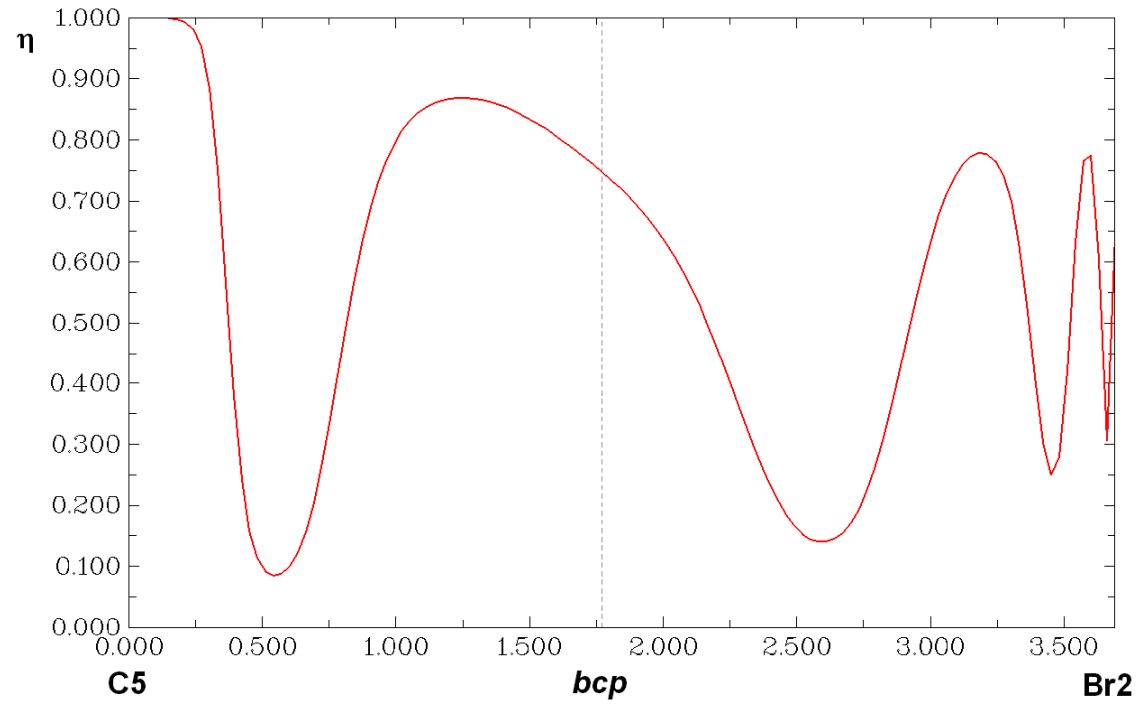
η
1.000
0.900
0.800
0.700
0.600
0.500
0.400
0.300
0.200
0.100
0.000
0.000 0.500 1.000 1.500 2.000 2.500 3.000 3.500
C5
bcp
Br2

(c)

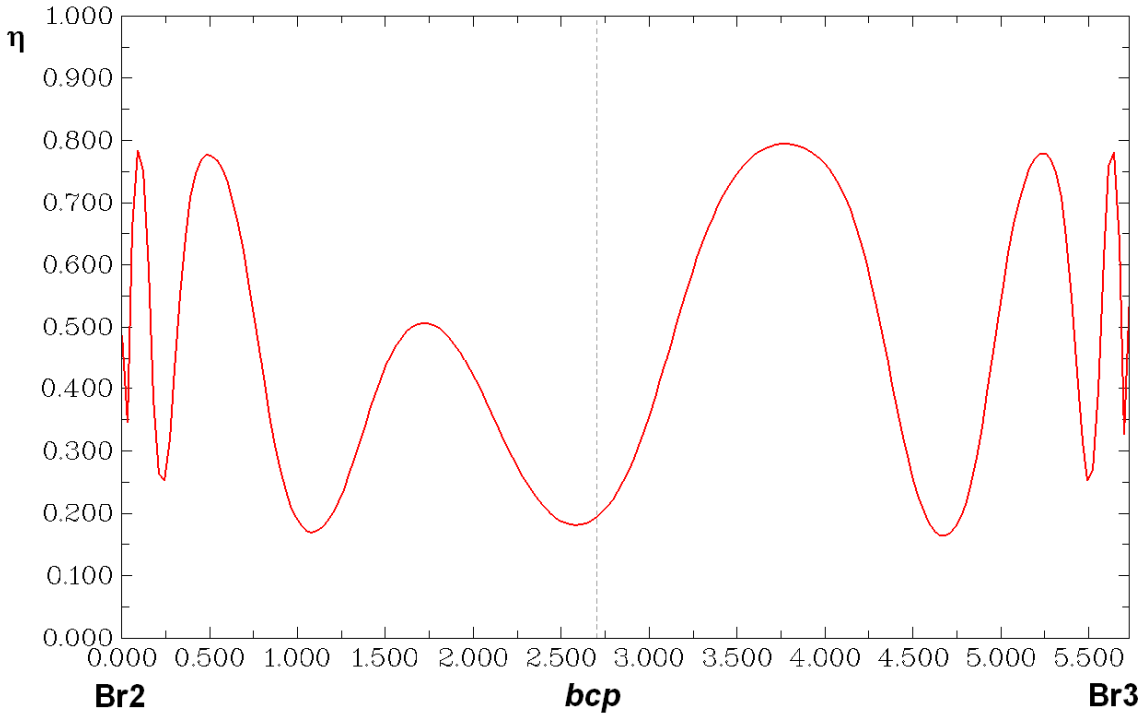
η
1.000
0.900
0.800
0.700
0.600
0.500
0.400
0.300
0.200
0.100
0.000
0.000 0.500 1.000 1.500 2.000 2.500 3.000 3.500 4.000 4.500 5.000 5.500
Br2
bcp
Br3

(d)

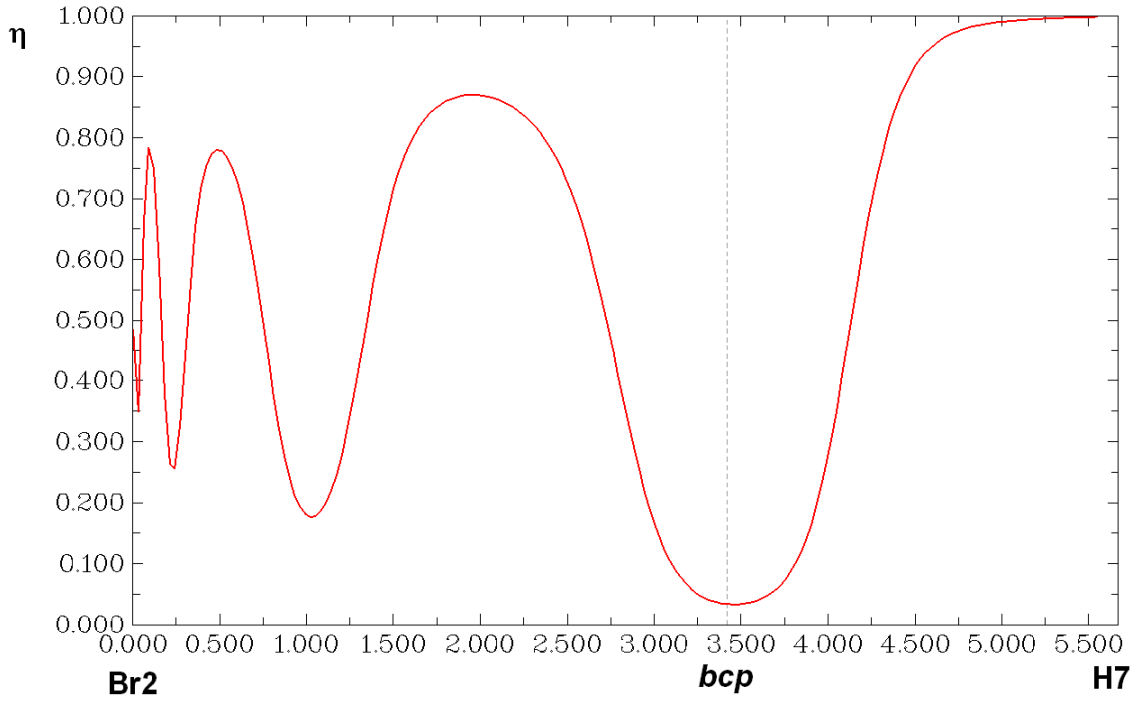
η
1.000
0.900
0.800
0.700
0.600
0.500
0.400
0.300
0.200
0.100
0.000
0.000 0.500 1.000 1.500 2.000 2.500 3.000 3.500 4.000 4.500 5.000 5.500
Br2
bcp
H7

(e)

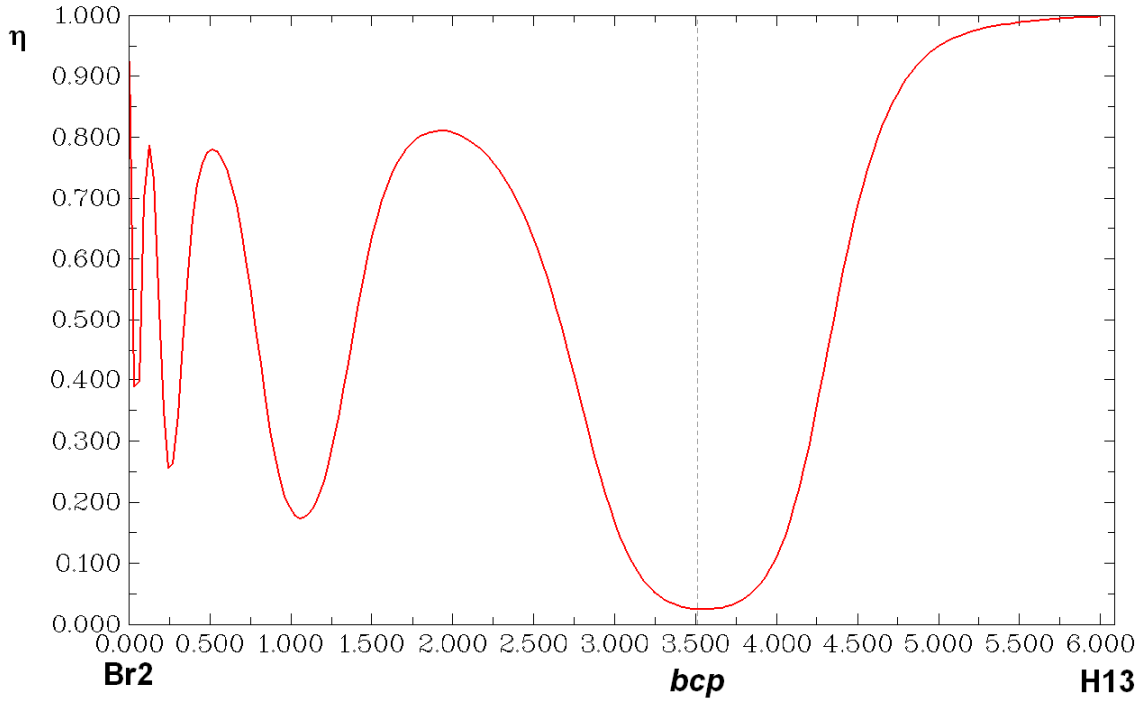
η
1.000
0.900
0.800
0.700
0.600
0.500
0.400
0.300
0.200
0.100
0.000
0.000 0.500 1.000 1.500 2.000 2.500 3.000 3.500 4.000 4.500 5.000 5.500 6.000
Br2
bcp
H13

Figure S4

Negative one-electron potential (in a.u.) along several bond paths of complex **1**. The location of bond critical points is shown by a dotted vertical line (distances in bohrs): (a) C5–Br1, (b) C5–Br2, (c) Br2···H7, and (d) Br2···H13.

(a)

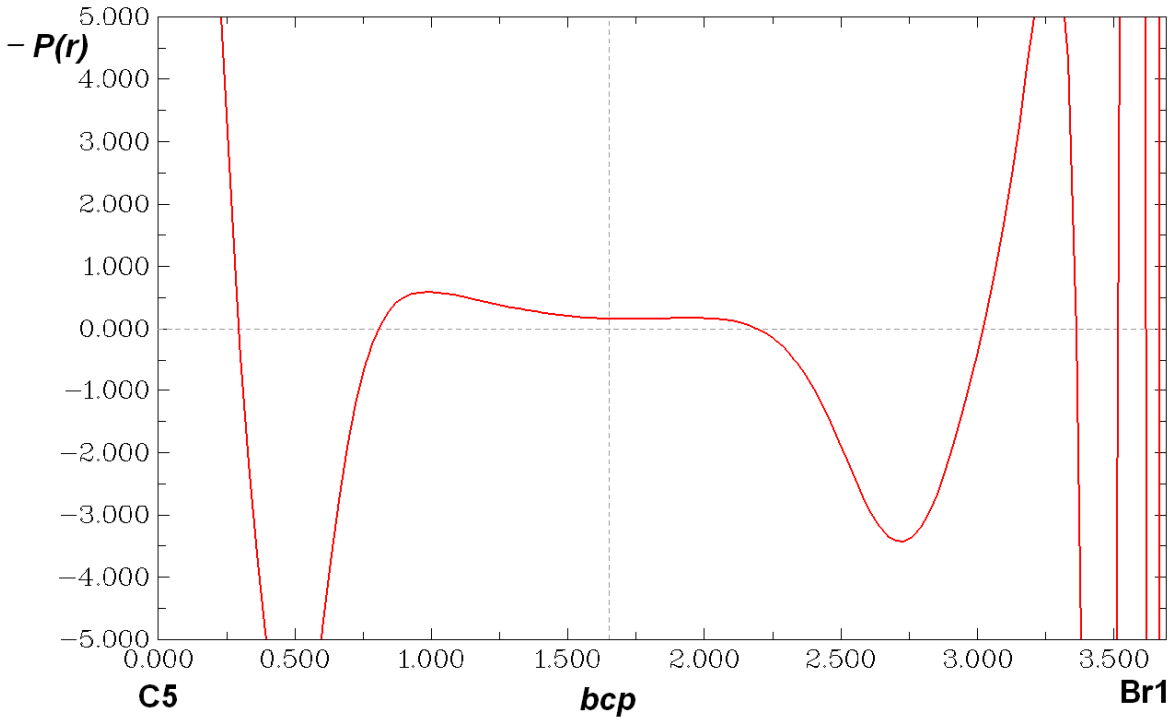

(b)

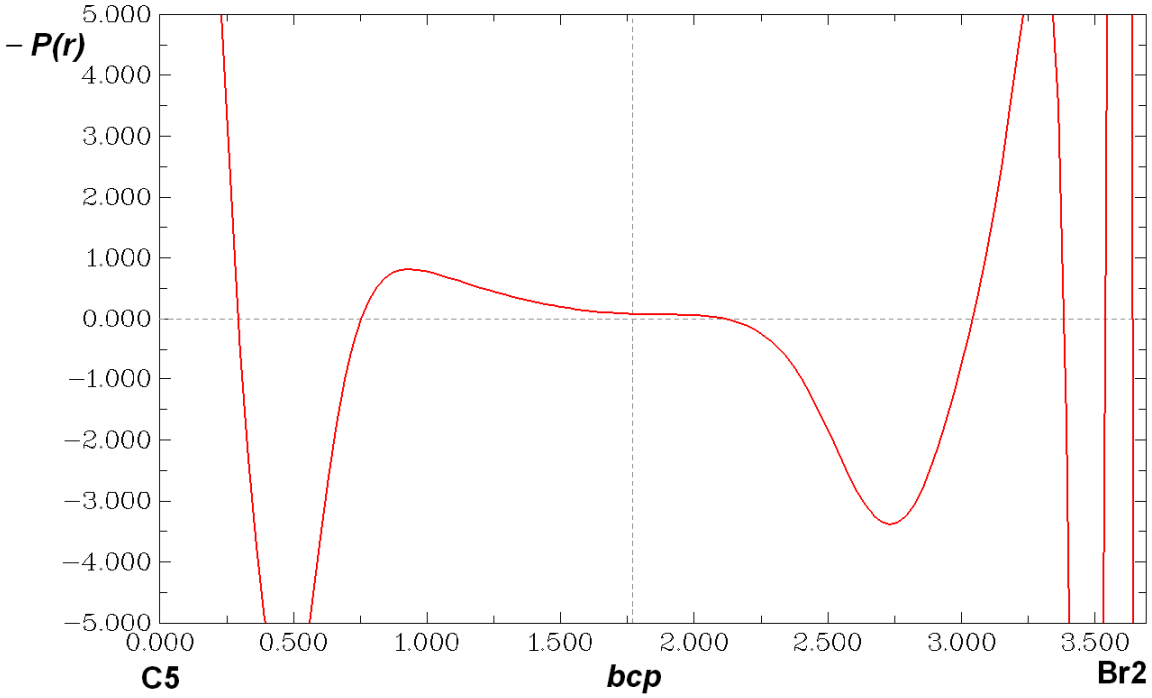
− P(r)
5.000
4.000
3.000
2.000
1.000
0.000
−1.000
−2.000
−3.000
−4.000
−5.000
0.000
0.500
1.000
1.500
2.000
2.500
3.000
3.500
C5
bcp
Br2

(c)

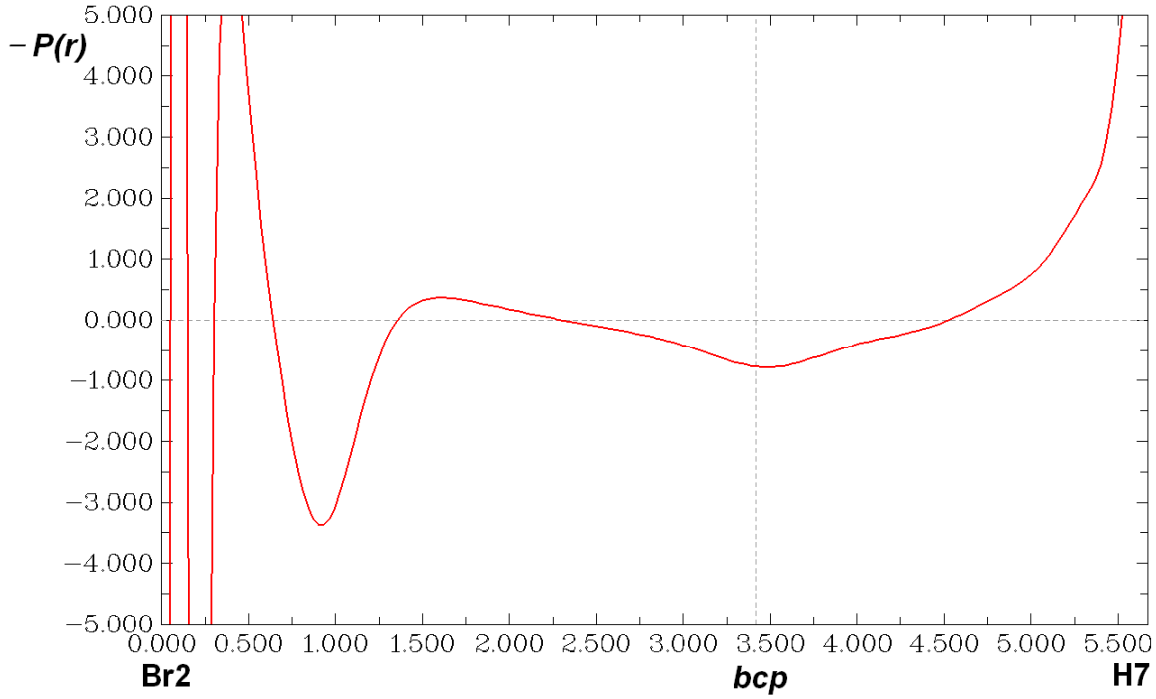
− P(r)
5.000
4.000
3.000
2.000
1.000
0.000
−1.000
−2.000
−3.000
−4.000
−5.000
0.000
0.500
1.000
1.500
2.000
2.500
3.000
3.500
4.000
4.500
5.000
5.500
Br2
bcp
H7

(d)

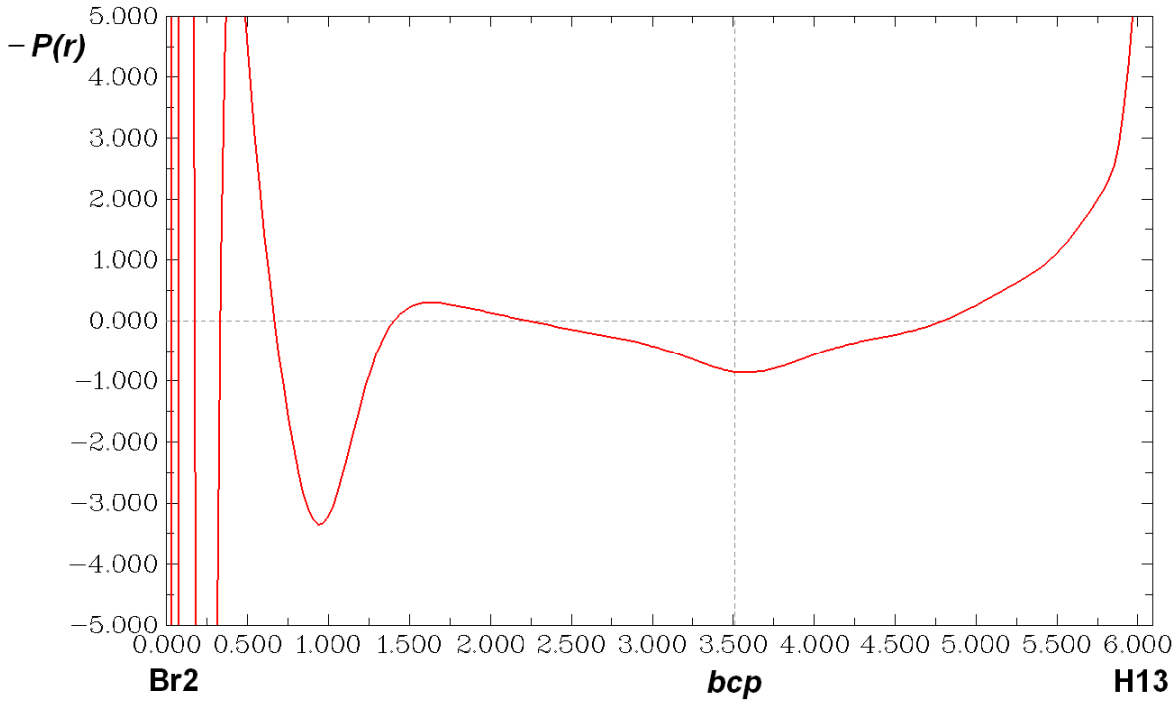
−P(r)
5.000
4.000
3.000
2.000
1.000
0.000
−1.000
−2.000
−3.000
−4.000
−5.000
0.000 0.500 1.000 1.500 2.000 2.500 3.000 3.500 4.000 4.500 5.000 5.500 6.000
Br2
bcp
H13

Figure S5

Laplacian of the electron density (in a.u.) along several bond paths of complex **1**, calculated using model 3 (equivalent results for model 4). The location of bond critical points is shown by a dotted vertical line (distances in bohrs): (a) C5–Br1, (b) C5–Br2, and (c) Br2···Br3.

(a)

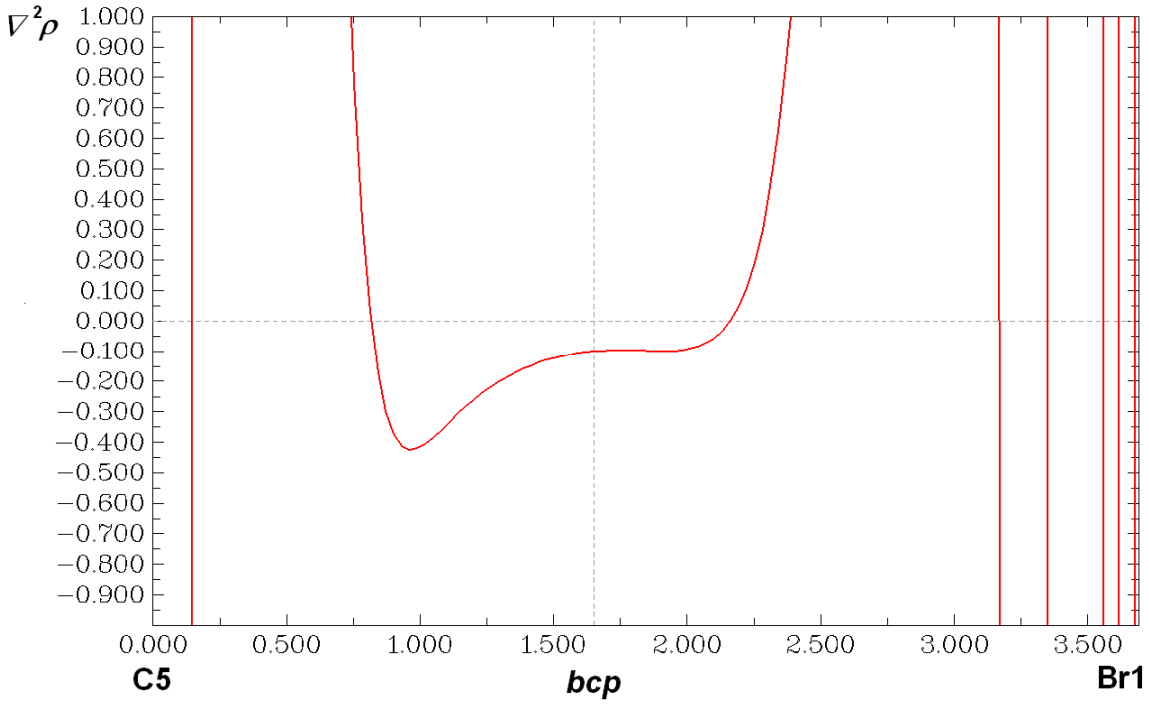

(b)

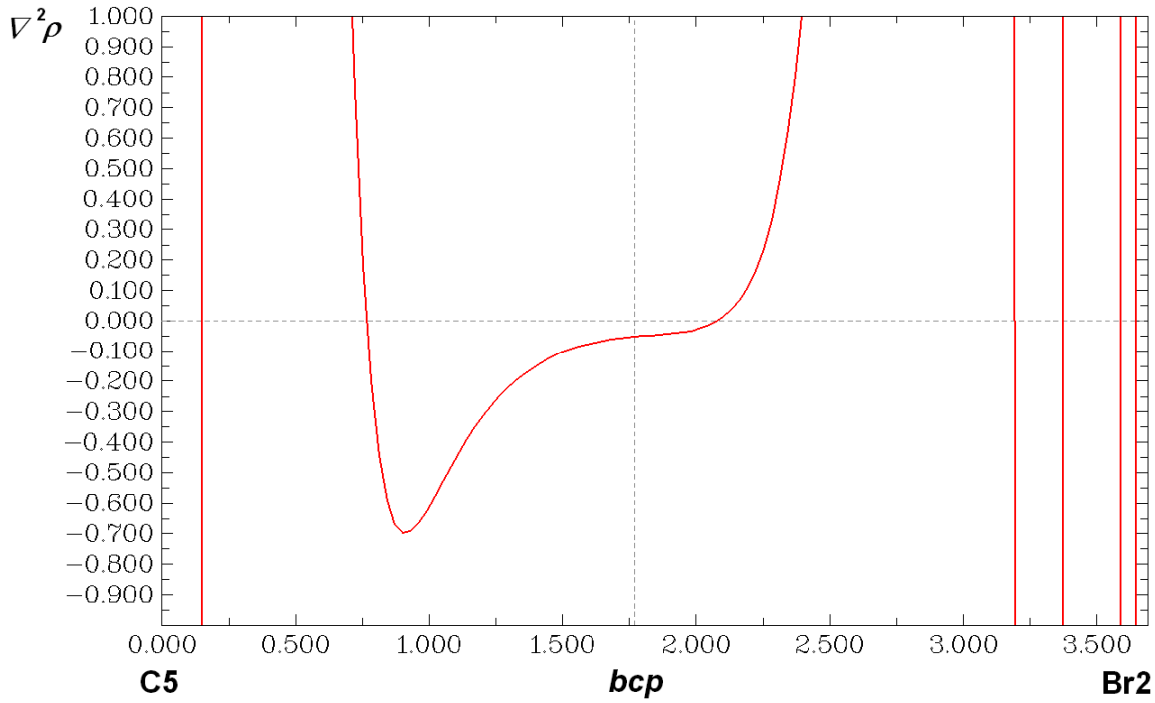
$\nabla^2\rho$
1.000
0.900
0.800
0.700
0.600
0.500
0.400
0.300
0.200
0.100
0.000
−0.100
−0.200
−0.300
−0.400
−0.500
−0.600
−0.700
−0.800
−0.900
0.000 0.500 1.000 1.500 2.000 2.500 3.000 3.500
C5
bcp
Br2

(c)

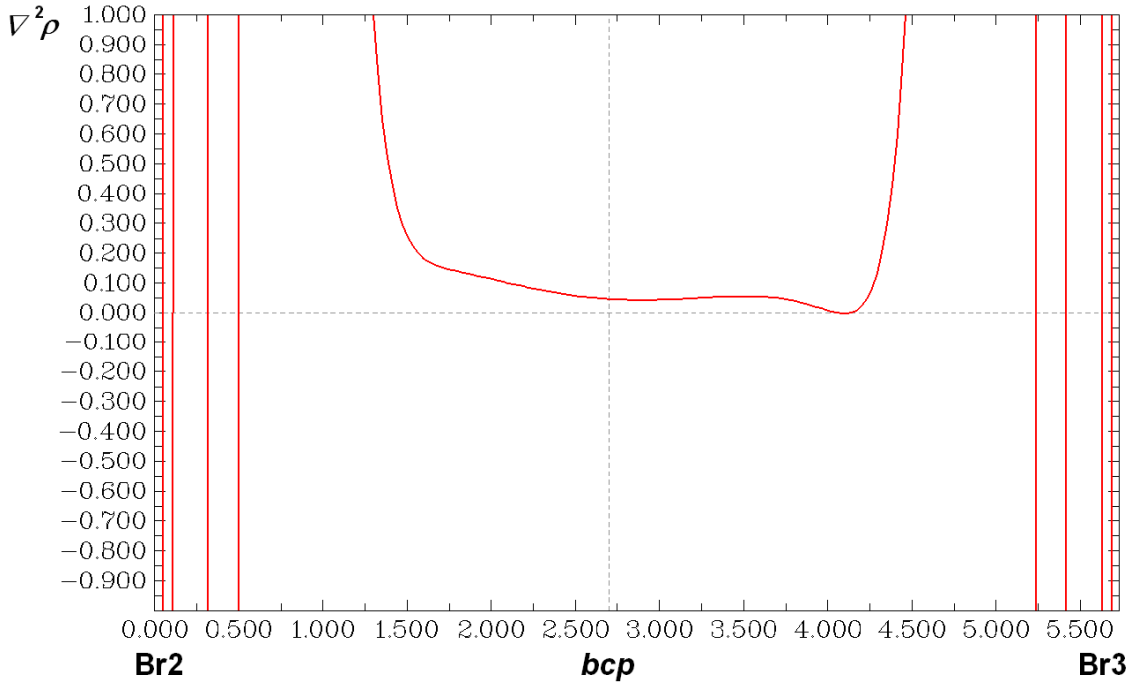
$\nabla^2\rho$
1.000
0.900
0.800
0.700
0.600
0.500
0.400
0.300
0.200
0.100
0.000
−0.100
−0.200
−0.300
−0.400
−0.500
−0.600
−0.700
−0.800
−0.900
0.000 0.500 1.000 1.500 2.000 2.500 3.000 3.500 4.000 4.500 5.000 5.500
Br2
bcp
Br3

Table S1

Cartesian coordinates of complex **1** (experimental geometry).

Atom	x	y	z
Mn	19.0962	15.2664	10.4983
C	19.7698	13.6179	9.8692
O	20.1994	12.6643	9.5017
C	18.3926	16.9028	11.0378
O	17.949	17.905	11.2993
C	18.995	15.8772	8.7647
O	19.0043	16.2539	7.7227
C	20.8362	15.844	10.5469
O	21.9025	16.1254	10.484
S	16.4857	13.2957	12.1719
C	17.5292	14.1693	13.3279
Br	16.7948	15.9571	13.7487
Br	17.3669	13.1133	15.0058
Br	16.7183	11.4103	17.4927
P	16.979	14.3226	10.386
C	16.8446	13.0012	9.1469
C	16.8324	13.3487	7.7977
H	16.787	14.2485	7.5671
C	16.8842	12.4189	6.8052
H	16.8447	12.6863	5.9153
C	16.9922	11.122	7.109
H	17.0568	10.4912	6.4288
C	17.0077	10.7168	8.4182
H	17.0452	9.8084	8.6143
C	16.9679	11.6576	9.4805
H	17.0223	11.3847	10.368
C	15.5192	15.359	10.0489
C	14.2645	14.9725	10.4651
H	14.1469	14.1902	10.954
C	13.1817	15.7719	10.141
H	12.3472	15.5339	10.4757
C	13.2622	16.8494	9.387
H	12.4959	17.3218	9.1535
C	14.4909	17.2604	8.9541
H	14.5697	18.0373	8.449
C	15.624	16.5181	9.2682
H	16.4566	16.7927	8.9581
P	19.259	14.4883	12.6995
C	20.1692	12.9207	12.7697
C	21.569	13.0098	12.7777
H	21.9913	13.8323	12.878
C	22.3118	11.8452	12.6329
H	23.2405	11.8933	12.6326
C	21.6993	10.6229	12.4899
H	22.2063	9.8527	12.3689
C	20.3475	10.5563	12.5279

H	19.9366	9.7246	12.4631
C	19.555	11.6866	12.6601
H	18.6279	11.6161	12.6746
C	20.0711	15.4932	13.9946
C	20.4071	16.8377	13.7085
H	20.1974	17.2253	12.8894
C	21.0534	17.5452	14.6871
H	21.3278	18.4141	14.501
C	21.3062	17.0409	15.8953
H	21.6942	17.5684	16.5556
C	20.9809	15.7161	16.1521
H	21.1862	15.3418	16.9783
C	20.3537	14.9489	15.1872
H	20.1298	14.0638	15.364

Table S2

Cartesian coordinates of complex **1** (theoretically optimized geometry: B3P86-D3(BJ)/6-31G(d,p) method).

Atom	x	y	z
Mn	19.1043861793	15.2036537807	10.4782038233
C	19.9157417562	13.6477575351	9.9349413709
O	20.4710611652	12.7313598781	9.5301044053
C	18.2759086868	16.7915380364	10.9180964007
O	17.8303932447	17.8383572778	11.0563019262
C	19.1010803147	15.7218960083	8.7609141443
O	19.14921236	16.0610148927	7.6603757654
C	20.7205311876	15.9264444761	10.807391852
O	21.7583928874	16.3800286545	11.0081897433
S	16.5234297154	13.1195269619	12.0403957988
C	17.4210126922	14.052977716	13.2520205782
Br	16.6289063291	15.8257941339	13.5735114249
Br	17.4602094324	12.8938369297	15.1110192073
Br	17.6890074399	11.5521333391	17.2762492747
P	17.0123539458	14.2147471198	10.2759720967
C	16.8733159151	12.9390339344	8.9885834662
C	16.1333323348	13.1454938106	7.8208269991
H	15.573042272	14.064684881	7.6838511233
C	16.1051574665	12.160438928	6.8366968497
H	15.5290658935	12.3244743142	5.9307372473
C	16.8031551453	10.9684839896	7.0162046476
H	16.7763510453	10.2020850778	6.2470798397
C	17.5298460892	10.755480081	8.1871693801
H	18.0676803792	9.8240671078	8.3361656874
C	17.5679063747	11.7356906984	9.1723219051
H	18.1274924009	11.5620746819	10.0879335154
C	15.6706979319	15.4031239348	9.9566444797
C	14.5526211827	15.4949134171	10.7890676226
H	14.4542086462	14.8362360335	11.645217611
C	13.5762817905	16.4544411078	10.5325958366
H	12.7139802953	16.5263836417	11.188647101
C	13.7045409197	17.3179253464	9.4476239105
H	12.9409754989	18.0658375575	9.2545857437
C	14.8177009792	17.226869068	8.6132606386
H	14.9257077831	17.8985693772	7.7668038807
C	15.8021166986	16.2783578786	8.870000806
H	16.6657203982	16.2167387126	8.2149503333
P	19.1303349373	14.3950689659	12.6811556735
C	20.0983559723	12.8590361386	12.7463236911
C	21.4869825651	13.0211203682	12.6459132923
H	21.917927468	14.0195349882	12.6327782977
C	22.3181709936	11.9095242705	12.5753807939
H	23.3933298475	12.04473183	12.503052651
C	21.7696978426	10.6280747131	12.6066871865
H	22.4177736943	9.7579644136	12.5555708608
C	20.3914731569	10.4656398697	12.7180176643

H	19.9612389151	9.4698959951	12.7675838983
C	19.550650367	11.574736142	12.7858476427
H	18.484540093	11.4318291244	12.90559989
C	19.893443592	15.4188394142	13.960931576
C	20.0027077046	16.8037612628	13.8133041892
H	19.672046754	17.2874520488	12.9017406518
C	20.5251071916	17.5759321669	14.8449455394
H	20.6098622964	18.6516038044	14.7227774547
C	20.9298659659	16.9677094153	16.0317531346
H	21.3327259007	17.5717982638	16.8397946357
C	20.8137455152	15.5875167394	16.1864525749
H	21.1151383549	15.1115693518	17.1144221084
C	20.3014926798	14.8081776294	15.1547333395
H	20.1947634145	13.7369127635	15.2857768168

Table S3

Cartesian coordinates of complex **1** (theoretically optimized geometry: ZORA-BLYP-D3(BJ)/TZP method).

Atom	x	y	z
Mn	19.21119	15.5453	11.15428
C	20.25499	14.67259	12.42747
O	20.9922	14.23145	13.19188
C	18.25828	16.454	9.83685
O	17.79991	17.10764	9.00659
C	20.76213	15.95216	10.2896
O	21.75969	16.24835	9.77998
C	19.27783	17.04768	12.1929
O	19.36362	17.99505	12.8503
S	17.28923	12.43987	10.66289
C	16.25016	13.70544	11.33892
Br	15.31712	14.77331	9.9224
Br	14.76807	12.58619	12.58915
Br	13.08313	11.30319	14.14171
P	18.96192	13.57149	9.93959
C	20.26807	12.30953	10.10291
C	21.08202	11.94354	9.02341
H	20.92763	12.3897	8.04749
C	22.08086	10.98613	9.20285
H	22.70704	10.70389	8.36136
C	22.26717	10.38688	10.44905
H	23.0444	9.63917	10.58264
C	21.44629	10.7412	11.52351
H	21.57835	10.27105	12.49357
C	20.45	11.69736	11.35385
H	19.80529	11.95821	12.18717
C	18.74457	13.7941	8.13991
C	17.65064	13.23249	7.4712
H	16.91339	12.6638	8.02722
C	17.50314	13.4232	6.09695
H	16.64632	12.99204	5.5875
C	18.44328	14.16777	5.38393
H	18.32233	14.31749	4.31433
C	19.53755	14.72794	6.04807
H	20.273	15.31006	5.50025
C	19.68689	14.54857	7.42156
H	20.53998	14.98911	7.92522
P	17.24899	14.89674	12.31743
C	17.74102	14.08341	13.87655
C	18.12371	14.94038	14.92317
H	18.00966	16.01509	14.81479
C	18.63362	14.41446	16.10772
H	18.91966	15.08553	16.91244
C	18.76545	13.03235	16.26096
H	19.15736	12.62228	17.18785
C	18.37629	12.17946	15.22754

H	18.4491	11.10269	15.34966
C	17.86903	12.69716	14.03613
H	17.54784	12.02442	13.25152
C	16.09369	16.1859	12.86408
C	16.05324	17.44373	12.24821
H	16.74714	17.68775	11.45274
C	15.10985	18.38734	12.64679
H	15.08684	19.36153	12.16722
C	14.19541	18.07517	13.65557
H	13.45681	18.81068	13.96387
C	14.22709	16.81979	14.26679
H	13.51111	16.56867	15.04351
C	15.17436	15.87397	13.88082
H	15.19191	14.89685	14.35097

Table S4

Bond distances and bond paths lengths for selected interactions of **1**, calculated using the four models[†].

Interaction	$D_{A–B}$(Å)[a]	$d_{A–B}$(Å)[b]	$d_{A–bcp}$(Å)[c]	$d_{bcp–B}$(Å)[d]
Br2···Br3	2.626	2.627	1.255	1.372
	2.557	2.558	1.220	1.338
	3.083	3.084	1.455	1.629
	3.083	3.084	1.478	1.606
Br2···H7	2.936	3.026	1.837	1.189
	2.867	2.992	1.790	1.202
	2.944	3.045	1.836	1.209
	2.944	2.997	1.844	1.153
Br2···H13	2.912	3.072	1.805	1.267
	2.837	2.953	1.774	1.179
	3.044	3.261	1.871	1.390
	3.044	3.221	1.875	1.346

[†]Models: ZORA-BLYP-D3(BJ)/TZP//ZORA-M06-2X/QZ4P (*model 1*, first row of each entry), B3P86-D3(BJ)/6-31G(d,p)//M06-D3/QZVP (*model 2*, second row of each entry), exp-geom//M06-D3/QZVP (*model 3*, third row of each entry), exp-geom//XCW-B3LYP/6-31G(d,p) (*model 4*, fourth row of each entry). [a]Bond distance. [b]Bond path length. [c]Distance from atom A to the bcp. [d]Distance from atom B to the bcp.